



NTNU – Trondheim
Norwegian University of
Science and Technology

Doped carbon nanostructures as metal-free catalysts for oxidative dehydrogenation of light alkanes

Kaia Andersson Jenssen

Chemical Engineering and Biotechnology

Submission date: June 2014

Supervisor: Magnus Rønning, IKP

Co-supervisor: Andrey Volynkin, IKP

Navaneethan Muthuswamy, IKP

Marthe Emelie Buan, IKP

Norwegian University of Science and Technology

Department of Chemical Engineering

Preface

This master`s thesis is submitted as the final part of the Master of Technology Degree in Chemical Engineering (MTKJ) at the Norwegian University of Science and Technology, and is a result of both experimental work and literature studies. The scientific work was carried out in a period of 20 weeks, in the spring of 2014.

First of all I would like to thank Professor Magnus Rønning, who has been supervising this project. I would also like to give many thanks to all of my co-supervisors. Post.doc fellow Navaneethan Muthuswamy for all of his help and enthusiasm regarding all aspects of this project, and Ph.D. candidate Marthe Emelie Melandsø Buan for helping me with the characterization procedures, and letting me use her results in my thesis. To be allowed to join your meetings have been valuable and much appreciated. Ph.D. candidate Andrey Volynkin also deserves many thanks, for his help both with the dehydrogenation setup, both practically and theoretically, during the last year.

Further, I would like to thank my fellow students, friends and family for the support during this work, and making my years in Trondheim unforgettable. I would especially like to thank Camilla Lindgren and Jørgen Nordbø, the process of writing this thesis would definitely not be the same without you!

In addition I would like to give special thanks to Simen Høy Aasheim, for all of his support and patience during all my years as a student. Now it is your turn!

I declare that this is an independent work, according to the exam regulations of the Norwegian University of Science and Technology (NTNU).

Place and date:

Trondheim, June 30th, 2014



Kaia Andersson Jussen

Abstract

Catalytic reactions are often carried out on various supported metals, these usually being noble metals or metal oxides. Even though metal based catalysts play a major role in today's industrial processes, they still have several disadvantages, including high cost, proneness to gas poisoning, as well as disadvantageous effect on the environment. Recently, certain carbon nanomaterials have been in the spotlight of several research groups, as carbon has the advantages of wide availability, environmental acceptability, corrosion resistance, in addition to its unique surface properties. The goal is to use the carbon nanomaterials to produce better catalysts - without the use of noble metals.

By doping carbon nanofibers and carbon nanotubes with other elements, one can significantly alter their physical and chemical properties, thus making them more reactive. Boron, nitrogen and phosphorus are some of the chemical elements that can be used as doping agents.

In this study nitrogen doped carbon nanofibers was investigated, by using them in the oxidative dehydrogenation (ODH) of propane. The carbon nanofibers was synthesized by chemical vapor deposition (CVD), where ammonia and various carbon (CO, C₂H₆, C₂H₄) sources was decomposed over on Fe or Ni, supported on expandable graphite. After the synthesis, the nitrogen doped carbon fibers was treated with nitric acid to remove the metal from the growth catalyst, before the sample was annealed. Three iron based samples was compared during this project; the as synthesized CNFs, the CNFs after acid treatment, and the CNFs after annealing. In addition a sample of as synthesized nickel based catalyst was investigated.

In addition to the activity testing, BET, XRD, TEM and XPS were carried out on the catalysts, which confirmed that the synthesis of the nitrogen doped carbon nanofibers was successful.

The results from the ODH suggests that the nickel based catalyst have better activity than the iron based samples, in addition to producing less CO₂. However, the selectivity towards propene was better for the iron based samples. This could be due to the differences in structure for the iron based and the nickel based catalyst, causing a difference in the distribution of nitrogen and oxygen groups on the surface.

Sammendrag

Katalytiske reaksjoner blir ofte utført ved hjelp av ulike metallkatalysatorer, bestående av finfordelt metall på en egnet bærer, der metallene som brukes er ofte edelmetaller og/eller metalloksider. Selv om metallbaserte katalysatorer spiller en stor rolle i dagens industri, har de flere ulemper knyttet til seg. Disse ulempene inkluderer høye kostnader, sårbarhet for gassforgiftning og ufordelaktige effekter på miljøet.

I de senere årene har flere forskningsgrupper fått interesse for karbonnanomaterialer. Karbon innehar flere fordeler; det er lett tilgjengelig, miljøvennlig, motstandsdyktig ift korrosjon og innehar unike overflateegenskaper. Målet er å bruke karbonnanomaterialer til å produsere bedre katalysatorer, uten bruk av dyre edelmetaller.

Ved doping/dotering av karbonnanofibre med andre stoffer, kan man endre de fysiske og kjemiske egenskapene til karbonfibrene drastisk, og blant annet gjøre dem mer reaktive i kjemiske reaksjoner. Bor, nitrogen og fosfor er eksempler på stoffer som er blitt brukt som doteringsstoffer.

I denne studien har nitrogendopede karbonnanofibre blitt studert, ved å bruke dem til oksidativ dehydrogenring av propan. Karbonfibrene ble syntetisert ved hjelp av kjemisk dampavsetning, der ammoniakk og ulike karbonforbindelser (CO , C_2H_6 , C_2H) ble nedbrutt over jern eller nikkel, på en bærer av grafitt. Etter syntetiseringen ble karbonnanofibrene behandlet med salpetersyre, før prøven ble varmebehandlet. Tre karbonprøver med jern som vekstkatalysator ble sammenlignet i løpet av dette forsøket: Ubehandlete nitrogendopede karbonnanofibre, den samme prøven etter syrebehandling, og igjen etter varmebehandling. I tillegg ble en ubehandlet prøve med nikkel som vekstkatalysator testet.

I tillegg til forsøk med oksidativ dehydrogenering, ble BET, XRD, TEM og XPS utført på prøvene, og bekreftet av syntesen av karbon nanofibre var vellykket.

Resultatene fra ODH antyder at den nikkelbaserte katalysatoren har en høyere aktivitet enn de jernbaserte prøvene, i tillegg til å produsere mer CO_2 . Samtidig ser selektiviteten for propen ut til å være høyere for de prøvene som ble syntetisert med jern som vekstkatalysator. Dette kan ha en sammenheng med de ulike strukturene i de jernbaserte og nikkelbaserte prøvene, som igjen resulterer i en forskjell i fordelingen av nitrogen- og oksygen grupper på overflaten.

Contents

Preface	i
Abstract	iii
Sammendrag	v
Symbols and abbreviations	xi
List of figures and tables	xiii
1. Introduction	1
1.1 Propene production	1
1.2 Metal free catalysts	1
1.3 Scope of work	2
2. Theory	3
2.1 Catalysis	3
2.2 Carbon fibers	5
2.3 Carbon as support for noble metals	5
2.4 Carbon nanotubes as metal free catalysts	6
2.5 Catalytic dehydrogenation of alkanes	7
2.5.1 Oxidative dehydrogenation of propane	9
2.7 Chemical Vapor Deposition	10
2.8 Characterization	10
2.8.1 Scanning Electron Microscopy and Transmission electron microscopy	10
2.8.2 The Brunauer-Emmet-Teller Method	10
2.8.3 X-Ray Diffraction	13
2.8.4 X-ray Photoelectron Spectroscopy	15
2.8.5 Thermogravimetric analysis	16
2.9 Gas Chromatography	17
2.9.1 Data analysis – converting signals from the gas chromatograph	17
3. Materials and methods	20

3.1 Synthesis of CNF`s	20
3.1.1 Nitrogen doped CNFs	20
3.1.2 Acid treatment and annealing of N-CNFs.....	20
3.1.3 Annealing of acid treated N-CNFs.....	21
3.2 Characterization of samples.....	22
3.2.1 Scanning Electron Microscopy, Transmission Electron Microscopy and X-ray Photoelectron Spectroscopy	22
3.2.2 X-Ray Diffraction	22
3.2.3 The Brunauer-Emmet-Teller Method	23
3.2.4 Thermogravimetric analysis.....	23
3.3 Oxidative dehydrogenation of propane	24
3.3.1 Data analysis	25
4. Results	26
4.1 Characterizations	26
4.1.1 SEM and TEM images	26
4.1.2 BET results.....	29
4.1.3 XRD results.....	31
4.1.4 X-ray Photoelectron Spectroscopy results	33
4.1.5 TGA results	34
4.3 Oxidative dehydrogenation.....	35
4.3.1 Conversions.....	35
4.3.2 Selectivity for propene	37
4.3.3 Selectivity for CO ₂	38
4.3.4. Selectivity for H ₂ O.....	39
5. Discussion	40
5.1 Synthesis	40
5.2 Catalyst characterization.....	40

5.2.1 BET	40
5.2.2 XRD	41
5.3 Activity measurements	41
6. Conclusions and future work.....	44
6.1 Synthesis and characterizations	44
6.2 Activity and selectivity measurements	44
6.3 Further work	45
7. References	46
Appendix A – Risk assessments.....	I
Appendix B – Raw data from the gas chromatograph	VI
Appendix C – ODH results	XVII
Appendix D - Mass flow controller calibrations	XVIII
Appendix E - Calibration curves and response factors	XX
Appendix F – BET-Isotherms	XXVII

Symbols and abbreviations

Symbol	Unit	Description
A_0	mol/s, mL STP/min	Surface area of one adsorbate molecule in BET measurements
A_i	mol/s, mL STP/min	Response of component i in GC measurements
A_{IS}	mol/s, mL STP/min	Response of the internal standard in GC
A		Total surface area in BET measurements
BET		Brunauer Emmett and Teller
CNF	J/K	Carbon nanofiber
CNT	g, mg	Carbon nanotube
CVD		chemical vapor deposition
DSC	mol ⁻¹	Differential Scanning Calorimetry
$F_{A,0}$	bar	Inlet molar flow of component A
F_A		Outlet molar flow of component A
F_i		Molar flow of component i
F_B		Outlet molar flow of component B
F_T	mmHg	Total molar flow
GC		Gas chromatography
GFCB		Gas Flow Controller Box
kB	μ Vs	Boltzmann constant
m	μ Vs	Mass, weight
MC		Mass spectroscopy
MFC	μ Vs	Mass Flow Controller
N_0	m ² /g	Number of molecules in a BET monolayer
N_A		Avogadro's number
NCNF		Nitrogen doped carbon nanofiber
NCNT		Nitrogen doped carbon nanotube
ODH		oxidative dehydrogenation
p		Adsorption pressure
P_0		Equilibrium, saturation pressure
PC		Pressure Controller
RF_i	mL	Response Factor of component i in GC measurements
RF_{IS}	mL STP/g cat	Response Factor of the internal standard in GC

		measurements
RRF _i	mL STP/g cat	Relative response factor of component i
S _{BET}	ml/mol	BET specific surface area
SEM		Scanning Electron Microscopy
STP	%	Standard temperature and pressure
SV		Safety Valve
TEM		Transmission electron microscopy
TC		Thermocouple
TCB		Temperature Controller Box
TGA	mL ⁻¹	Thermogravimetric analysis
V		Volume
V _a	mol/s, mL STP/min	Volume of adsorbed gas
V ₀	mol/s, mL STP/min	Volume of adsorbed gas in a monolayer
V _m	mol/s, mL STP/min	Molar volume of an ideal gas
Vulcan		A carbon black brand name
XA		Conversion of component A
XPS	J/K	X-ray photoelectron spectroscopy
XRD	g, mg	X-ray diffraction
Y _i		Gas phase mole fraction of component i.
YIS	mol ⁻¹	Gas phase mole fraction of the internal standard
α	bar	Slope value in the BET equation
χ		Ratio of desorption rate constants for the 2nd and 1st adsorption layer
3VW		Three-way-valve

List of figures and tables

Figure 2. 1: Catalytic cycle..	3
Figure 2.2: Potential energy diagram for a heterogenic catalytic reaction.....	4
Figure 2.3: Different forms of carbon structures.....	5
Figure 2.4: Oxidative dehydrogenation of alkanes, on functionalized carbon nanofibers.....	7
Figure 2.5: The five different types of adsorption isotherms.....	12
Figure 2.6: Simplified representation of the X-ray Diffraction set up.....	13
Figure 2.7: Schematic of how the X-rays are diffracted when they hit the sample surface.....	14
Figure 2.8: The four different nitrogen species found in NCNTs.....	15
Table 3.1: Summary of the nitrogen doped carbon nanofibers used in this project.....	21
Figure 3.1: Sample holder for the XRD analysis	22
Figure 3.2: Flow chart of the oxidative dehydrogenation apparatus.....	24
Figure 4.1: SEM images of nitrogen doped carbon nanotubes	26
Figure 4.2: The difference in structure for Fe-NCFs and Ni-FCNFs	27
Figure 4.3: Illustration of tip-growth in Fe-NCFs and Ni-NCFs.	28
Figure 4.4: Isotherms from the BET analysis of NCF31, NCF31-N and NCF31-N-900, including linear regression lines and formulas.	29
Table 4.1: BET surface areas for the samples NCF31, NCF31-N and NCF31-N-900.....	30
Figure 4.5: X-ray Diffraction scans for XRD scans for NCF31, NCF31-N, NCF31-N-900, NCF29 and expandable graphite.....	31
Figure 4.6: XPS scans for NCF31, NCF31-N and NCF31-N-900.....	33
Table 4.2: Nitrogen/carbon and oxygen/carbon ratios for the samples.....	33
NCF31, NCF31-N and NCF31-N-900	33
Figure 4.7: TGA results for NCF31 and NCF31-N.	34
Figure 4.7: Conversion of propane for NCF31, NCF31-N, NCF31-N-900 and NCF29.	36
Figure 4.8: Selectivity for propane for NCF31, NCF31-N, NCF31-N-900 and NCF29.	37
Figure 4.9: Selectivity for CO ₂ for NCF31, NCF31-N, NCF31-N-900 and NCF29.	38
Figure 4.10: Selectivity for H ₂ O for NCF31, NCF31-N, NCF31-N-900 and NCF29.	39
Figure A.1: Risk assessment, part 1	I
Figure A.2: Risk assessment, part 2	II
Figure A.3: Risk assessment, part 3	III
Figure A.4: Risk assessment, part 4	IV
Figure A.5: Risk assessment, part 5	V

Table B.1: Raw data from the gas chromatograph for parallel 1, NCF31	VI
Table B.2: Raw data from gas chromatograph for parallel 2, NCF31-N.....	VIII
Table B.3: Raw data from gas chromatograph for parallel 3, NCF31-N-900.....	X
Table B.3: Raw data from gas chromatograph for parallel 4, NCF29	XII
Table B.5: Raw data from gas chromatograph for the blank test.....	XIV
Table B.6: Raw data from gas chromatograph for Vulcan carbon.....	XV
Figure C.1: Conversion of propane for Vulcan Carbon.....	XVII
Figure C.2: Selectivity for propane for Vulcan Carbon.....	XVII
Figure D.1: MFC calibration, propane.....	XVIII
Figure D.2: MFC calibration, Synthetic Air	XVIII
Figure D.3: MFC calibration, Nitrogen, upper MFC	XIX
Figure D.4: MFC calibration, Nitrogen, lower MFC	XIX
Table E.2: Volume percentages and corresponding areas from the GC for nitrogen	XX
Figure E.1: Calibration curve for nitrogen	XX
Table E.2: Volume percentages and corresponding areas from the GC for propane.....	XXI
Figure E.2: Calibration curve for propane.....	XXI
Table E.3: Volume percentages and corresponding areas from the GC for propene.....	XXII
Figure E.3: Calibration curve for propene.....	XXII
Table E.4: Volume percentages and corresponding areas from the GC for CO	XXIII
Figure E.4: Calibration curve for CO.....	XXIII
Table E.5: Volume percentages and corresponding areas from the GC for CO ₂	XXIV
Figure E5: Calibration curve for CO ₂	XXIV
Table E.6: Volume percentages and corresponding areas from the GC for Synthetic Air .	XXV
Figure E.6: Calibration curve for propene.....	XXV
Table E.7: Response Factors for the different gases	XXVI
Figure E.1: BET isotherms for NCF31, NCF31-N and NCF31-N-900.	XXVII

1. Introduction

1.1 Propene production

Propene is, among other lower olefins, one of the most important feedstocks for the chemical industry. In spite of this, the main source of propene is as a side product of other processes, and consequently the availability of propene is largely determined by the demand of the main products.

The production of lower olefins, like ethane and propene, is mainly achieved by steam cracking of ethane, propane, naphtha or liquefied petroleum gas (LPG) [1]. Even though the process of steam cracking can give high yields toward unsaturated hydrocarbons, the process is highly energy consuming, partly due to the high temperatures needed in the process [1].

Because using ethane as a feedstock for cracking is less expensive and thus more often used, the propene production is reduced [2]. This, combined with the increase in consumption of propene due to the production of polypropylene, has raised an interest for a dedicated production of propene. Oxidative dehydrogenation of propene is one of the processes of interest [3].

1.2 Metal free catalysts

The dehydrogenation of propene is usually carried out in the presence of metal catalysts, often containing noble metals.

Even though metals and metal oxides are the most widely used catalysts in many industrialized processes, the metal based catalysts often suffer from several disadvantages. This disadvantages includes high cost, poor selectivity and durability, and also detrimental environmental effects [4]. Because of these shortcomings, it is very much desirable to develop cheaper, metal-free alternatives, which still maintain a high performance and stability.

The recent availability of carbon nanomaterials of various types, including fullerenes, carbon fibers and –nanotubes, carbon diamonds and grapheme sheets, offer new opportunities for developing advanced carbon-based catalysts without the involvement of noble materials, and a lot of research have been done on the topic of metal-free catalysts [4-7] .

1.3 Scope of work

One way of altering the properties of the carbon nanofibers, is to introduce doping agents, and in this way enhance the surface activity of the carbon fibers. Nitrogen as a doping agent has been widely studied, with good results [5, 8], and the scope of this work is to synthesize nitrogen doped carbon nanofibers, characterize them, and study their reactivity in the oxidative dehydrogenation of propane. The nitrogen doped carbon nanofibers will be further treated with acid as well as annealed, and the reactivity of the samples will be compared. In addition to the oxidative dehydrogenation reaction several characterization methods will be used to investigate the samples.

2. Theory

2.1 Catalysis

Catalysis is the increase in rate of a chemical reaction, due to the involvement of a substance called a catalyst. The catalyst forms bond with the reacting molecules of the reaction, and allow these to reacts to form a product, which then detaches from the catalyst. The catalyst is thus left unaltered, and is available for the next reaction. In figure 2.1, the catalytic reaction from reactants A and B to product P are shown. A and B binds to the catalyst, before they react within this complex to form the product P. P then separates from the catalyst, leaving the catalyst ready to perform the cycle again.

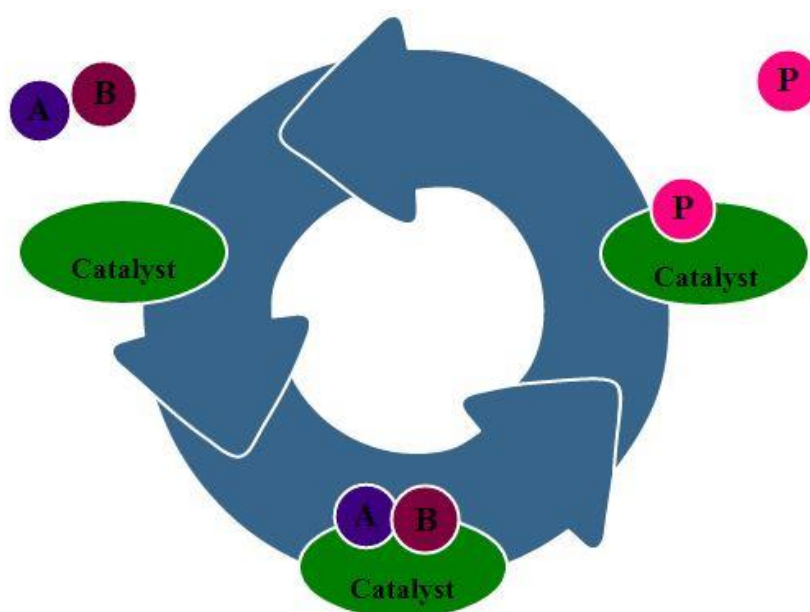


Figure 2. 1: Catalytic cycle. Reactants A and B form the product P with help from the catalyst.

The catalyst speeds up the reaction by lowering the energy barrier of the reaction. The difference between the potential energy for a catalyzed and non-catalyzed reaction are shown in Figure 2.2 [9]. For an uncatalyzed reaction the reaction proceeds when the reactants bump in to another with sufficient energy to overcome the activation barrier. The catalytic reaction on the other hand, starts with a spontaneous binding of the reactants to the catalyst surface. The formation of the reactant-catalyst complex is thus exothermic, and the Gibbs free energy is lowered. The reaction of A and B on the catalyst are associated with an activation energy,

but this is significantly lower than it would be for an uncatalyzed reaction. The last step is the separation of the product from the catalyst surface, which is an endothermic step.[9]

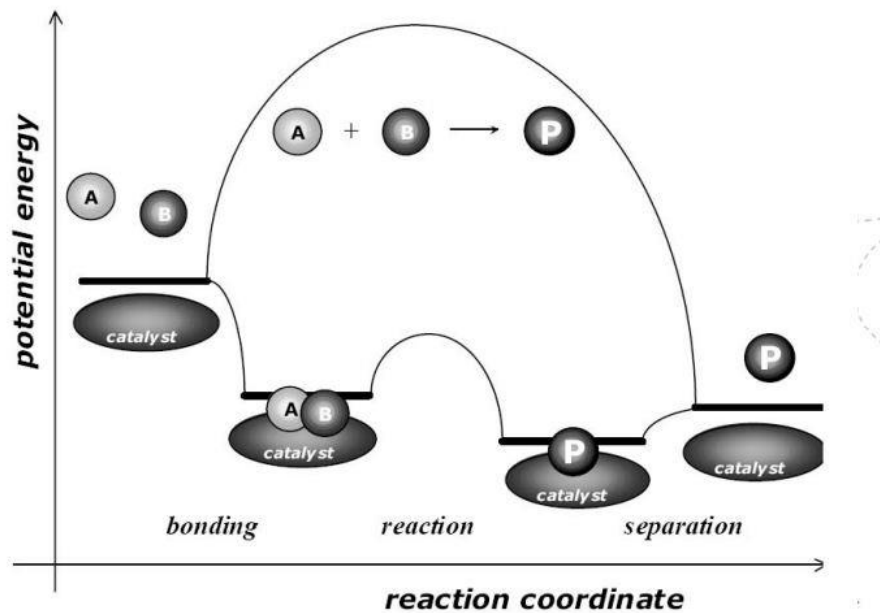


Figure 2.2: Potential energy diagram for a heterogenic catalytic reaction.[9]

To be successful, a catalyst has to possess several qualities. It has to have a high activity, but also a high selectivity towards the desired products, so as few unwanted by products as possible is generated. The catalyst also needs to stay active over time, and be possible to regenerate[9]. For a catalyst to be active, it has to possess active sites on the surface, necessary for adsorption of reactants, bond breaking and –formation, as well as desorption of the finished products. [4] to ensure that the catalytic activity remains effective over a long period, an excellent structural stability is also crucial.

A catalyst can be made of virtually any type of material, for example metals, metal oxides, sulfides, carbides, nitrides, acids or salts. They can also be gases and liquids, as well as solids. Solid catalysts also comes in various forms, such as loose particles, or particles on a support.[9]

2.2 Carbon fibers

Carbon fibers have been in use for a long time. They were patented already in 1880, by Thomas Edison, who used carbon fibers as one of the materials during his development of the incandescent lamp [10]. Carbon nanofibers can be defined as sp^2 -based linear filaments, with a diameter of ca. 100 nanometers, whilst regular carbon fibers have diameters of several micrometers [11]. Figure 2.3 shows the structural difference between different forms of carbon structures. Whereas carbon nanofibers can be seen as regularly stacked conical layers along the fiber length, the carbon nanotubes consist of a single hollow tube, with one or more walls. In addition, several other structures can form, as is also shown in the figure [11, 12].

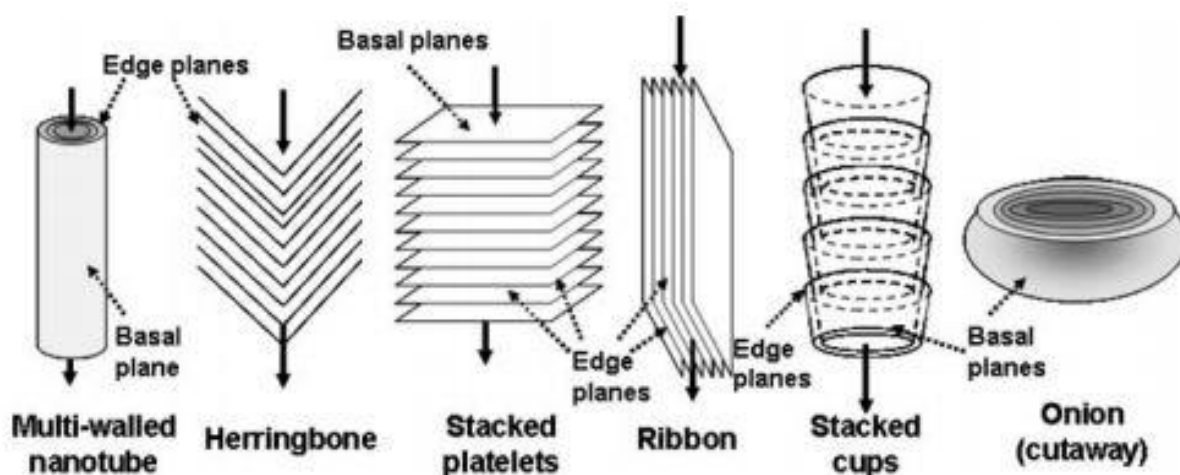


Figure 2.3: Different forms of carbon structures [12].

2.3 Carbon as support for noble metals

A good catalyst support usually has a high surface area, high porosity, and good thermal stability as well as high mechanical strength, to withstand crushing and attrition.[9] For low temperature hydrogenation catalysis, carbon is the support of choice[9]. Porous carbons can be used in hydrogenation reactions of organic compounds, as a support for noble materials. Active carbons can be prepared from pyrolysis, from for example wood, coal or coconut shells. [9]

2.4 Carbon nanotubes as metal free catalysts

At the time being, metals and metal oxides are the most commonly used catalysts in the industry, and noble metals, such as Pt, Pd and Rh, are widely used [4]. As well as their high cost, these metal-based catalysts suffer from several other disadvantages, such as poor durability and low selectivity[4]. In addition, disadvantageous environmental effects can be caused both by catalyst residues and undesirable side-products [4]. Because of this, it is very much desirable to develop cheaper, metal-free alternatives, which still have high performance. The recent availability of carbon nanomaterials of various types, including fullerenes, carbon fibers and –nanotubes, carbon diamonds and grapheme sheets, offer new opportunities for developing advanced carbon-based catalysts without the involvement of noble materials[4].

The electronic structure, defect sites and surface chemistry are highly relevant when it comes to catalytic performance, and thus the introduction of surface heteroatoms into carbon nanomaterials could further cause electron modulation, to provide desirable electronic structures for various catalytical processes. Doped carbon materials have thus found various applications in the field of catalysis, both as metal-free catalysts, or as support for other catalytic units[4, 6].

By doping carbon fibers and nanotubes with heteroatoms one can significantly alter their physical, chemical and electronic properties, and thus modify the catalytic performance, by introducing electron acceptors and donors[7, 8]. Doping of carbon nanotubes with electron rich nitrogen for example, will provide additional electrons for the graphic lattice of the carbon, and give rise to metallic or semi-conductive features by narrowing the energy gap [8]. Together with nitrogen, boron and phosphorus are some of the chemical elements that can be used as doping agents. Both boron and nitrogen are neighbors of carbon on the periodic table, and can provide n- and p-doping respectively, since their valence electrons are in the second shell, as for carbon[7]. Phosphorus has its valence electrons in its third shell, and is therefore fundamentally different from nitrogen and boron. Whereas both nitrogen and phosphorus mostly acts as electron donors, boron, together with the other elements in group 13, have Lewis acidity-properties, thus acting as an electron acceptor[13]. Studies have demonstrated that both phosphorous and nitrogen can be homogeneously incorporated into the lattice of carbon nanotubes. Doping CNFs with large amounts of phosphorus can be challenging, because the phosphorous atoms are larger than the carbon atoms, thus increasing the disorder within the carbon framework[7]. Despite of these difficulties, growth of carbon nanotubes

with low levels of phosphorous leads to new perspectives towards controlling the electronic properties of CNFs.

2.5 Catalytic dehydrogenation of alkanes

Dehydrogenation is a chemical reaction, in which hydrogen is removed from another molecule. Catalytic dehydrogenation is a growing technology for the production of olefins especially for the production of propene [2]. The dehydrogenation of propane to make propene has become an important process, due to the shortage of propene. This shortage is increasing due to the large portion of steam crackers that are using the more inexpensive ethane as feedstock rather than larger alkanes, thus not producing propene as a side product [2].

Several studies have been performed on various types of doped carbon fibers as catalysts for oxidative dehydrogenation of alkanes [8, 14], and promising results have been found, even though the activity still is not comparable to the metal catalysts.

The surface of carbon nanomaterials typically contains a variety of oxygen functional groups. The ketonic and quinoidic groups within the surface species contain a lot of electrons, and therefore contain a great potential to coordinate redox reactions. This is of relevance for the production of alkenes, since the Lewis basic sites can abstract hydrogen atoms from the C-H bonds in alkane molecules, and by this produce the corresponding alkene. Oxygen molecules adsorb on to the surface of the carbon material, and dissociate. When the alkane molecule also adsorbs on to the surface the C-H bond breaks and the hydrogen reacts with the dissociated oxygen to form water. The reaction is shown in Figure 2.4 [15], and is also written as equation (2.5) in chapter 2.6.1.

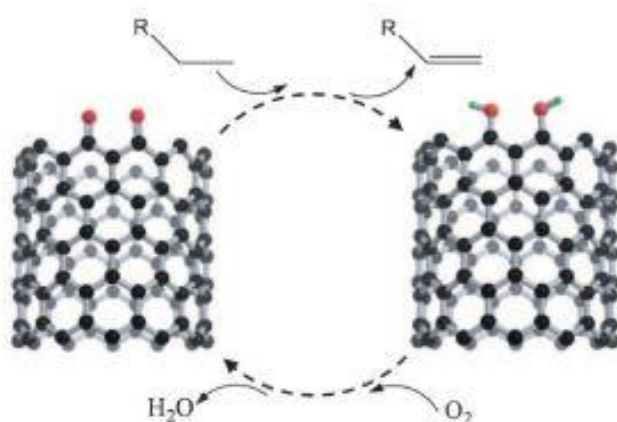


Figure 2.4: Oxidative dehydrogenation of alkanes, on functionalized carbon nanofibers

Recent studies have found that nano-scale carbon materials show good performances in the oxidative dehydrogenation of hydrocarbons. The nanocarbons are well adaptable to kinetic and mechanistic researches of complex redox reactions, which provides for great possibilities to investigate the nature of ODH reactions on a fundamental level. [15]

Studies have shown that CNTs doped with boron and phosphorous have better selectivity towards propene compared to original CNTs. This improvement could be due to the improved chemical stability after the modification[15].

Studies have found a propene selectivity of 40-60% for both doped and un-doped carbon nanofibers [8, 16].

A correlation between the oxygen reduction reaction and oxidative dehydrogenation have been found, but whether the correlation was due to a shared active site between the ORR and ODH reactions or if the reactions are correlated through the nanostructure of the carbon alone, was not determined[17].

2.5.1 Oxidative dehydrogenation of propane

Non catalytic propane dehydrogenation is an endothermic process, and requires high temperatures to achieve a high yield. Catalytic dehydrogenation on the other hand are endothermic, thus opening for the possibility of much lower reaction temperatures [18].

During non-oxidative dehydrogenation of propane, the following reactions take place:



Where reaction 2.1 is the main dehydrogenation reaction, and reaction 2.2-2.4 are the probable side reactions[18].

For oxidative dehydrogenation, the following set of equations is suggested:



Here reaction 2.5 is the oxidative dehydrogenation of propane, which is the preferable reaction. Reactions 2.6 and 2.7 are the oxidation of propane to CO_2 and CO respectively. Reaction 2.9 and 2.10 are the oxidation of propene to CO_2 and CO , whereas reaction 2.11 is the oxidation of carbon monoxide. The last reaction, 2.12 is the cracking of propane to form methane and ethene [19].

2.7 Chemical Vapor Deposition

Chemical vapor deposition (CVD) is a commonly used chemical process, for producing solid materials, high in both purity and performance. The majority of its applications involve applying thin films of solid coating to surfaces, but it can also be used to make high-purity bulk materials and powders, as well as producing composite materials. In typical CVD one or more precursor gases are flowed over the substrate that is to be coated [20].

As for the growing of carbon nanotubes (CNT`s), CVD is both a flexible and economically attractive method. Depending on the interaction between the catalyst and the support, two different growth mechanisms can occur; tip-growth and root growth. Tip-growth occur when the catalyst-support interaction are weak, and lifts the catalyst off the support while the CNT`s grow. For root growth on the other hand, the catalyst particles remain on the support while the CNT`s are growing, due to stronger interaction between the catalyst and the support [21].

2.8 Characterization

2.8.1 Scanning Electron Microscopy and Transmission electron microscopy

A scanning electron microscope (SEM) is a type of electron microscope that can produce images of a sample. The images are produced by “bombarding” the sample with electrons in a focused beam. By detecting the secondary electrons emitted by the atoms that are excited by the electron beam, an image of the surface of the sample is formed [22]. Transmission electron microscopy (TEM) works in a similar way, but where SEM is based on scattering of the electrons, TEM is based on transmitting electrons. The SEM can see contrast, due to the topology and surface of the sample surface, whereas TEM projects the information on the mass of the sample in a two-dimensional image, and can provide a more detailed picture.

2.8.2 The Brunauer-Emmet-Teller Method

The Brunauer-Emmet-Teller (BET) -equation was developed by Brunauer, Emmet and Teller, hence the name. The equation describes multimolecular adsorption on non-porous, solid surfaces, and the BET theory is an important analysis technique for measuring the specific surface area of materials [23].

The basic principle concerning surface area measurements are quite simple. By physisorption of an inert gas, usually N₂, to the surface of the sample, one can determine how many

molecules that are needed to form a complete monolayer, and thus find the surface area. The amount of adsorbed gas molecules depends on the relative vapor pressure of the gas, and is proportional to the total surface area of the material. The connection between the vapor pressure of the gas and the amount of adsorbed gas at a given temperature is called the adsorption isotherm [9, 23].

Even though this is straightforward in theory, in practice the molecules might not only adsorb to the surface in one layer, but adsorb beyond the monolayer to form one or more multilayers. If the sample contains small pores, the molecules might also condense inside the pores, filling them up. The narrower the pores are, the easier it is for the inert gas to condense in them[9].

There are several assumptions that govern the BET theory[9]. These assumptions are all given below:

- Equal adsorption- and desorption rate in any layer, i.e. dynamic equilibrium between adsorbate and adsorptive
- Molecules adsorb on equivalent adsorption sites in the first layer
- Molecules in the first layer establish the adsorption sites for the molecules in the second layer, and so on for the following layers
- Interactions between adsorbates are ignored
- The adsorption-desorption conditions are the same for all the layers except the first
- The adsorption energy for the molecules in the second and higher layers are the same as the condensation energy
- When the adsorption pressure approaches the saturation pressure, the multilayers grows to infinite thickness.

By applying these assumptions the BET equation can be derived:

$$\frac{P}{V_a(P - P_0)} = \frac{1}{xV_0} + \frac{(x-1) P}{xV_0 P_0} \quad (2.13)$$

Where P is the adsorption pressure, P₀ is the saturation pressure, V_a is the volume of the adsorbed gas, V₀ is the volume of gas adsorbed in the first monolayer, and x is the ratio of the desorption rate constants for the first and second layer.

Plotting $P/V_a(P-P_0)$ versus P/P_0 results in a straight line with a slope $\alpha = (x-1)/xV_0$, which crosses the x-axis at $\eta = 1/xV_0$.

The volume adsorbed in the first monolayer can then be found as

$$V_0 = \frac{1}{\alpha + \eta} \quad (2.14)$$

The volume V_0 can also be converted into the number of molecules adsorbed, by use of the ideal gas law:

$$N_0 = \frac{PV_0}{k_b T} \quad (2.15)$$

Where k_b is the Boltzmann constant and T is the temperature. Knowing how big an area each molecule of the inert gas occupies, (A_0), the total area can be found as $A = N_0 A_0$.

When the total area is found, the specific surface area, A_{BET} , can be found by dividing A with the sample mass of the catalyst.

Adsorption isotherms are divided into five categories, according to their shape. The different types are presented in Figure 2.5. Of these five, Type II are best fitted for use in the BET equation [24]

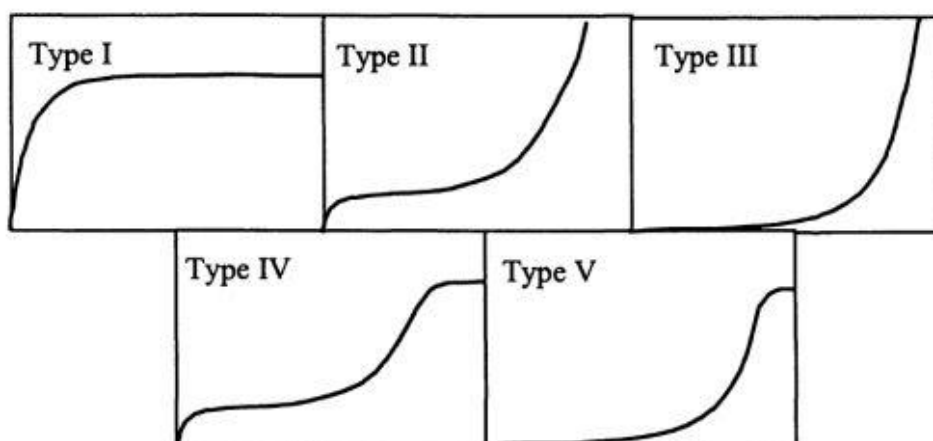


Figure 2.5: The five different types of adsorption isotherms [24].

2.8.3 X-Ray Diffraction

X-ray diffraction (XRD) is one of the oldest and most frequently used characterization methods used for catalysts. X-rays were discovered by Wilhelm Conrad Röntgen in the late nineteenth century, and powder diffraction was developed not long after, in 1985 [9, 25].

When sending a beam of X-rays on to the surface of a crystalline sample, the atoms in the sample cause the X-rays to diffract in different directions. The diffraction pattern acts as an individual fingerprint for any crystalline phase, and from this one can learn if the sample is crystalline, and which crystalline phases are present in the sample. If instead of a single crystal one wishes to analyze a sample consisting of fine powder, as is the general constitution of a catalyst, Powder X-ray Diffraction is used. The diffraction pattern acts as an individual fingerprint for any crystalline phase, and the powder diffraction is widely used to identify different phases in a mix, which generally constitutes a catalyst [22, 25].

A simplified representation of the X-ray diffraction set up is demonstrated in Figure 2.6. The divergent X-ray beam illuminates an area of the sample, which either decreases with increasing diffraction angle, or is kept constant by use of a variable slit opening. The reflected X-rays are then detected by a detector [22].

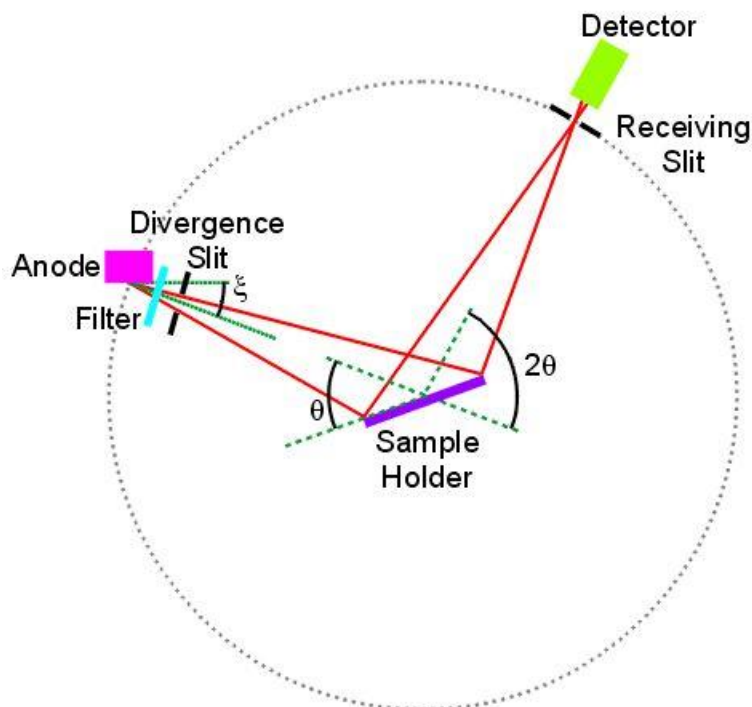


Figure 2.6: Simplified representation of the X-ray Diffraction set up. The X-ray beams hit the sample, and get reflected to the detector [26].

A figure showing how the X-rays are diffracted by the surface of the sample is shown in Figure 2.7. The X-ray beams have a wavelength λ when they are projected from the apparatus are projected on to the surface of the sample, which will reflect the x-ray beams. By measuring the angles of the diffraction, powder diffraction diagrams are obtained. The spacing d between two lattice planes, are related to the diffraction angle 2θ by Bragg's law [25, 27]:

$$n\lambda = 2d \sin \theta \quad (2.16)$$

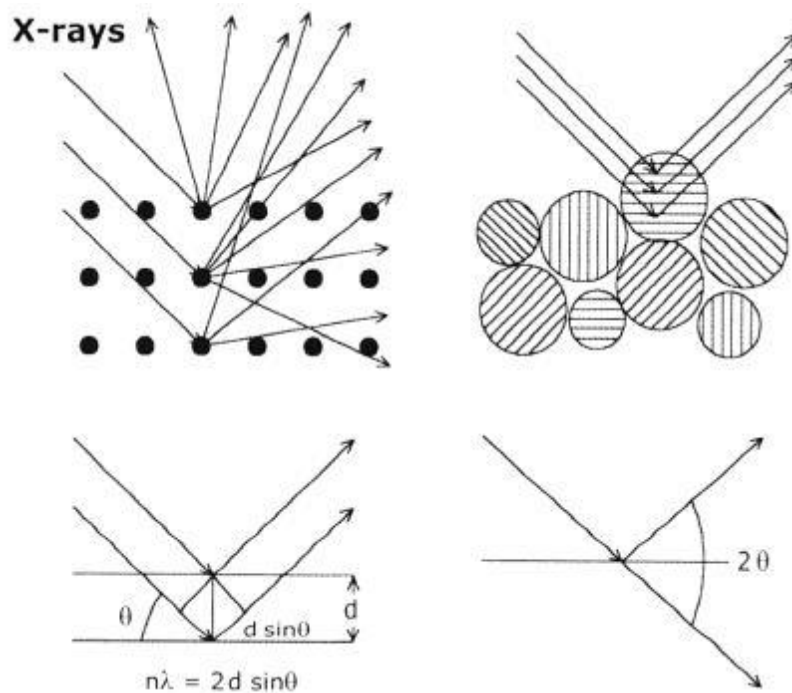


Figure 2.7: Schematic of how the X-rays are diffracted when they hit the sample surface.

It exist several databases that hold information about different crystal structures, which can be used to match the results from the XRD scans with known crystal structures. One example is the Powder Diffraction Files, maintained by the International Centre for Diffraction Data (ICDD) [28].

2.8.4 X-ray Photoelectron Spectroscopy

X-ray photoelectron spectroscopy (XPS) is among the most frequently used techniques in catalysis, and refers to the technique of bombarding the surface of the catalyst with X-ray photons, to produce the emission of characteristic electrons. This way one can measure the elemental composition of the material, including the oxidation states [9]

XPS are based on the photoelectric effect, where an atom absorbs a photon with a certain energy, so that a core- or valence electron is ejected with kinetic energy. The kinetic energy of the photoelectron can be written as:

$$E_k = h\nu - E_b - \phi \quad (2.17)$$

Where h is the Planck's constant, ν is the frequency of the exciting radiation (and thus $h\nu$ is the energy of the photon), E_b is the binding energy of the photoelectron, and ϕ is the work function of the spectrometer [9].

Nitrogen has four possible bonding configurations in graphitic networks [29], which are shown in Figure 2.8 [30]. The figure also shows the same bonding configurations incorporated in a carbon structure [12]. By use of the XPS, one can find which of the configurations is present in the sample, as well as their quantity.

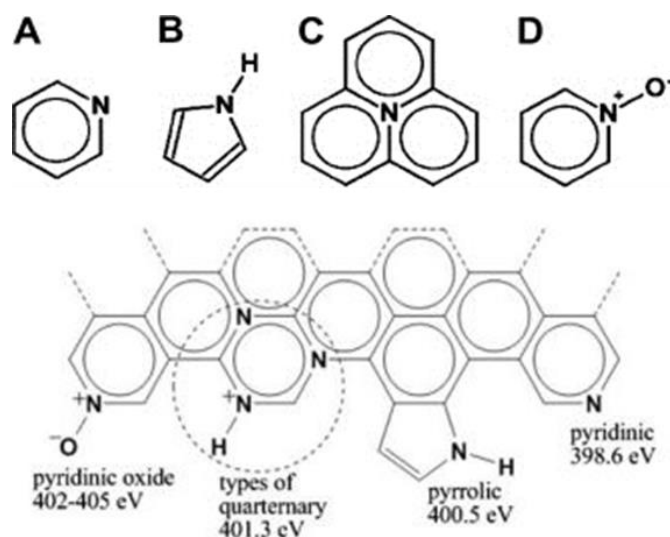


Figure 2.8: The four different nitrogen species found in NCNTs: (A) Pyridinic, (B) Pyrrolic, (C) Quaternary and (D) Oxidized pyridinic. The different bonding configurations are presented both alone and incorporated in a carbon structure [12, 30].

2.8.5 Thermogravimetric analysis

Thermogravimetric analysis (TGA) is a characterization technique where the mass of a substance is monitored as a function of either temperature or time, as the sample is subjected to a temperature controlled environment in a controlled atmosphere. Since the two methods have identical test conditions, and generally compliments each other, TGA is often coupled with Differential Scanning Calorimetry (DSC), in order to observe the heat development in the sample. TGA can also be coupled with for example mass spectroscopy (MS) and/or gas chromatography (GC) to analyze the off-gases produced during the temperature programmed treatment [31, 32].

2.9 Gas Chromatography

Chromatography is a separation technique, where the components of the sample that are to be separated are partitioned between two phases. One of the phases is stationary, whilst the other, the moving phase, can either be solved in a fluid or a gas. For gas chromatography (GC), the moving phase consists of the injected gas sample, together with an inert carrier gas. The stationary phase can be either a solid (gas-solid chromatography) or a liquid (gas-liquid chromatography), and the different components separate based on their affinities for the solid phase. This means that the components are eluted from the column at different times, and can thus be separated based on the elution time for each individual component[33].

For more rapidly analysis of gas mixtures, a Micro GC is often used. To achieve a fast and efficient separation, the Micro GC uses long capillary wall coated columns, together with a high flow of carrier gas [34].

2.9.1 Data analysis – converting signals from the gas chromatograph

For converting of the GC signals into gas flows, the method of internal standard (IS) is often used. This method involves a standard compound, the internal standard, which is added to the original sample. The internal sample has to be inert, and added in an accurately known concentration. Because the amount and composition of the internal standard is assumed to maintain constant throughout the experiment, it can be used as a reference for calculating the amount of the other components in the sample[34, 35].

A response factor for each of the components in the sample is also needed. The response factor characterizes the relation between the eluted amount of the solute and the peak area. The relation for component *i* are shown in equation 2.18, where A_i , RF_i and Y_i are the area, response factor and volume fraction of component *i* respectively.

$$RF_i = \frac{A_i}{Y_i} \quad (2.18)$$

The relative response factor for each component can be found by dividing the response factor of the component with the response factor for the internal standard. This is shown in Equation 2.19.

$$RRF_i = \frac{RF_i}{RF_{IS}} = \frac{A_i / Y_i}{A_{IS} / A_{IS}} = \frac{A_i}{A_{IS}} \frac{Y_{IS}}{Y_i} \quad (2.19)$$

The relative response factors are found by running samples with known volume percentages of each component together with the internal standard. Then the known volume percentages and the areas of the peaks found by the GC are inserted in the equation above, giving the relative response factor.

When the relative response factors for all the components are found, they can be used to find the volume percentages of components in the sample, as shown in Equation 2.20.

$$Y_i = \frac{A_i}{A_{IS}} \frac{Y_{IS}}{RRF_i} \quad (2.20)$$

The flow rates of the components are assumed to be proportional to the volume percentages. This means that the following relationship is valid:

$$\frac{F_i}{Y_i} = \frac{F_{IS}}{Y_{IS}} \quad (2.21)$$

Where F_i and F_{IS} are the flow rate of component i and the internal standard respectively. This can be rearranged to the following equation, to calculate the flow rate of component i .

$$F_i = \frac{Y_i \times F_{IS}}{Y_{IS}} \quad (2.22)$$

The conversion can then be calculated as in Equation 2.23 [3]:

$$\chi = \frac{F_i^{In} - F_i^{Out}}{F_i^{In}} \quad (2.23)$$

The selectivities for the different species can be calculated as shown in Equations 2.24-2.29 [3]. Two alternative equations for the selectivity of CO and CO₂ are given, as both the carbon balance and the oxygen balance can be used for gases containing both elements.

$$S_{C_3H_6} = \frac{F_{C_3H_6}^{Out}}{F_{C_3H_8}^{In} - F_{C_3H_8}^{Out}} \quad (2.24)$$

$$S_{CO_2} = \frac{1}{3} * \frac{F_{CO_2}^{Out}}{F_{C_3H_8}^{In} - F_{C_3H_8}^{Out}} \quad (2.25)$$

$$S_{CO_2} = \frac{F_{CO_2}^{Out}}{F_{O_2}^{In} - F_{O_2}^{Out}} \quad (2.26)$$

$$S_{CO} = \frac{1}{3} * \frac{F_{CO}^{Out}}{F_{C_3H_8}^{In} - F_{C_3H_8}^{Out}} \quad (2.27)$$

$$S_{CO} = \frac{F_{CO}^{Out}}{F_{O_2}^{In} - F_{O_2}^{Out}} \quad (2.28)$$

$$S_{H_2O} = \frac{1}{2} * \frac{F_{O_2}^{Out}}{F_{O_2}^{In} - F_{O_2}^{Out}} \quad (2.29)$$

3. Materials and methods

The risks and hazards associated with the experimental work were evaluated, and risk assessments made. The risk assessments are given in Appendix A. The biggest hazards concerning actual injury were determined to be contact with corrosive materials and liquid nitrogen. Gas leakages and exposure to flammable and/or toxic gases (C_3H_8 , CO, CO_2) were also considered a big hazard. To avoid injuries to skin and eyes, gloves, safety goggles and laboratory coats were used. To avoid gas leakages, hand held gas detectors were used to thoroughly check lines and junctions, and leak tests with pressures up to 2 bar were performed. In addition, permanently installed gas detectors are placed in every lab. The alarms all have a low and a high alarm, where the high alarm sets off the alarms in the whole building, as well as alert the fire department. For the oxidative dehydrogenation reaction the experiment is carried out inside a closed and ventilated glass cage, further preventing large gas leaks.

3.1 Synthesis of CNF`s

3.1.1 Nitrogen doped CNFs

The nitrogen-doped carbon nanofibers (N-CNFs) were grown by chemical vapor deposition (CVD), in a tubular quartz reactor. Ammonia and various carbon sources (CO, C_2H_6 , and C_2H_4) was decomposed over on Fe or Ni, supported on expendable graphite. The expanded graphite was made from oxidized graphite, which was heated in a microwave-oven at 700w for 60 seconds.

The growth catalyst was prepared by impregnating the expanded graphite with a solution of ethanol, containing either iron or nickel nitrate, before it was reduced in a H_2/Ar atmosphere at $650^\circ C$ for 3 hours. The N-CNFs were grown at $650^\circ C$ for 24 hours, in a gas flow containing carbon, nitrogen and hydrogen.

3.1.2 Acid treatment and annealing of N-CNFs

1 gram of the grown N-CNFs was heated to $110^\circ C$ in an oil bath, and treated with 50 ml nitric acid for 3 hours before it was transferred to a Buchner funnel and rinsed with distilled water. The procedure was repeated a total of three times.

3.1.3 Annealing of acid treated N-CNFs

0,31 grams of the acid treated N-CNFs was heated to 900°C for two hours in an argon atmosphere before it was allowed to cool down.

A total of four samples were prepared for further testing. These are summarized in Table 3.1.

Table 3.1: Summary of the nitrogen doped carbon nanofibers used in this project

Treatment	Metal used in growth catalyst	Name of sample
As synthesized	Ni	NCF29
As synthesized	Fe	NCF31
Acid treated	Fe	NCF31-N
Acid treated and annealed	Fe	NCF31-N-900

3.2 Characterization of samples

3.2.1 Scanning Electron Microscopy, Transmission Electron Microscopy and X-ray Photoelectron Spectroscopy

Due to time limitations, some priorities had to be taken regarding the characterization of the samples. Since TEM and XPS results already existed for the samples, it was chosen not to repeat these procedures. Thus, the TEM and XPS characterizations given in this report are carried out by PhD candidate Marte E. M. Buan at the catalysis group.

3.2.2 X-Ray Diffraction

The XRD samples were prepared by using high vacuum grease to fix the carbon material to the sample holders, see Figure 3.1. The experiment was done with a scan time of 30 minutes, with a 2-Theta angular range of 20-80 degrees and a fixed 6 mm illumination of the sample. The analysis was performed on NCF31, NCF31-N, NCF31-N-900, and NCF29, as well as on pure expandable graphite. To identify the different phases in the samples, the software DIFFRAC.EVA, including a data base of powder diffraction files (PDFs) was used.



Figure 3.1: Sample holder for the XRD analysis

3.2.3 The Brunauer-Emmet-Teller Method

The BET method was performed using a Micromeritics Tristar 3000 Surface Area and Porosity Analyser and a VacPrep 061 Degasser, with the purpose of determining the specific surface area of each sample.

The samples were weighed in a quartz sample tube, before they were installed in the degassing apparatus. All the samples were weighed twice, to obtain as accurate measurements as possible. Around 80mg of sample was used. The samples were left to degas overnight, at 200°C. The samples were then allowed to cool down to room temperature before they were placed in the BET apparatus. During the analysis the samples were submerged in liquid nitrogen, to maintain a constant temperature of 195,85°C.

The analysis was performed on NCF31, NCF31-N, and NCF31-N-900.

3.2.4 Thermogravimetric analysis

The thermogravimetric analysis (TGA) was performed using a Netzsch STA 449C apparatus, with the purpose of determining the weight-loss of the sample with increasing temperature.

The samples were weighed in a crucible before it was installed in the apparatus. A pre-programmed temperature program was run, and the samples were heated from room temperature up to 850°C.

The analysis was performed on the samples NCF31 and NCF31-N.

3.3 Oxidative dehydrogenation of propane

The activity of the samples NCF31, NCF31-N, NCF31-N-900 and NCF29 was tested by performing oxidative dehydrogenation of propane. Each sample was only tested once, due to the amount of sample available. In addition to the catalysts, a test with pure Vulcan Carbon was performed, as well as a “blind test” with only quartz wool in the reactor. To ensure that the calculations were as accurate as possible, the MFCs were calibrated with a bubble flow meter. The calibrations are given in Appendix B. In addition, calibration curves for both the feed gases and the possible products of the reaction were made. These are given in Appendix C.

A flow chart of the ODH setup is presented in Figure 3.2.

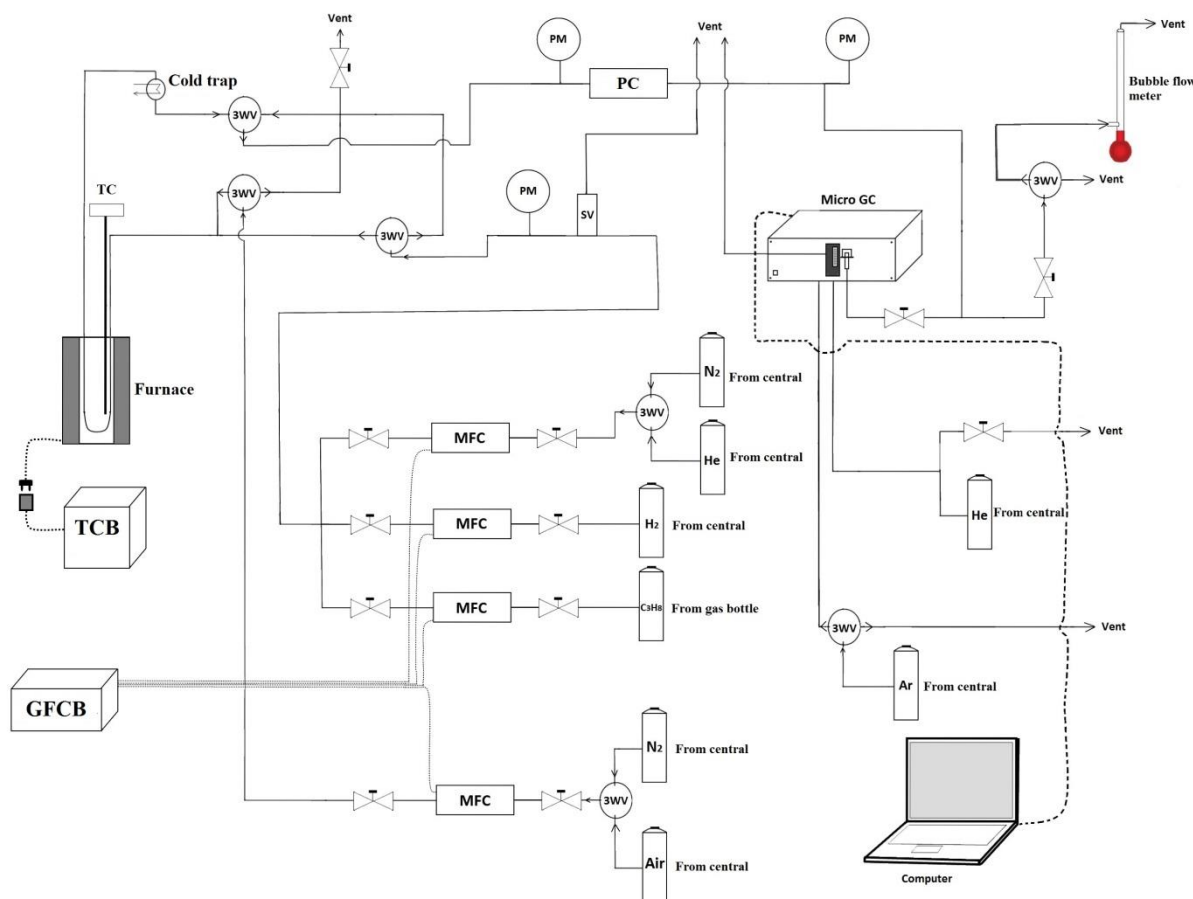


Figure 3.2: Flow chart of the oxidative dehydrogenation apparatus. GFCG: Gas flow controller box, TCB: Temperature controller box, MFC: Mass flow controller, 3WV: Three way valve, PC: Pressure controller, PM: Pressure meter, SV: Safety valve, TC: Thermocouple, GC: Gas chromatograph.

With the exception of propane, the gases are fed to the system from a central gas distribution system. The flow and composition of the feed are controlled by several mass flow controllers, and can either be sent to the reactor, or directly to the GC via a bypass system, using three way valves. The setup is equipped with a straight plug flow quartz reactor, with an inner diameter of 6 mm, placed inside an electrical furnace. A thermocouple is used to measure the temperature in the furnace, which are controlled by a temperature controller. A cold trap with cooling water is placed after the furnace to condense the water formed in the dehydrogenation reaction. To prevent the pressure in the system from building up, the setup is equipped with a safety valve, as well as several pressure meters. The gases are analyzed with micro gas chromatography, using a Agilent 3000A Micro GC containing four columns, each with a thermal conductivity detector (TCD).

The catalyst was placed inside the reactor, between two layers of quarts wool. The catalyst was heated until 400°C under N₂ atmosphere (100 ml/min). After reaching 400°C, a total flow of 33,3ml/min of C₃H₈, synthetic air and nitrogen (in the ratio 15:15:70 respectively) was fed into the reactor. Reaction conditions were maintained for the duration of 15-25 hours.

The product gas mixture was analyzed by gas chromatography, using nitrogen as an internal standard for the calculations. The feed was analyzed several times before being fed into the reactor, and this analyzes was used for calculation of the composition in the feed.

3.3.1 Data analysis

Before the data from the GC could be used, all of the peaks that where to be used in calculations had to be manually integrated, as the GC did not manage to draw correct baselines on its own. The manually integrated peaks are the ones presented as raw data in Appendix B.

The gas flows, conversion rates and selectivities was calculated from the equations in the theory. To find the exact flow rates for the internal standard, nitrogen, a calibration curve for nitrogen was used. The flow rates for propane were also found via the calibration curves, rather than via the response factors. The calibration curves are given in Appendix C.

4. Results

4.1 Characterizations

4.1.1 SEM and TEM images

Figure 4.1 shows the SEM image of sample of iron grown carbon nanofibers. These pictures confirm that the attempt to grow carbon nanofibers with various diameters on the expanded graphite support were successful.

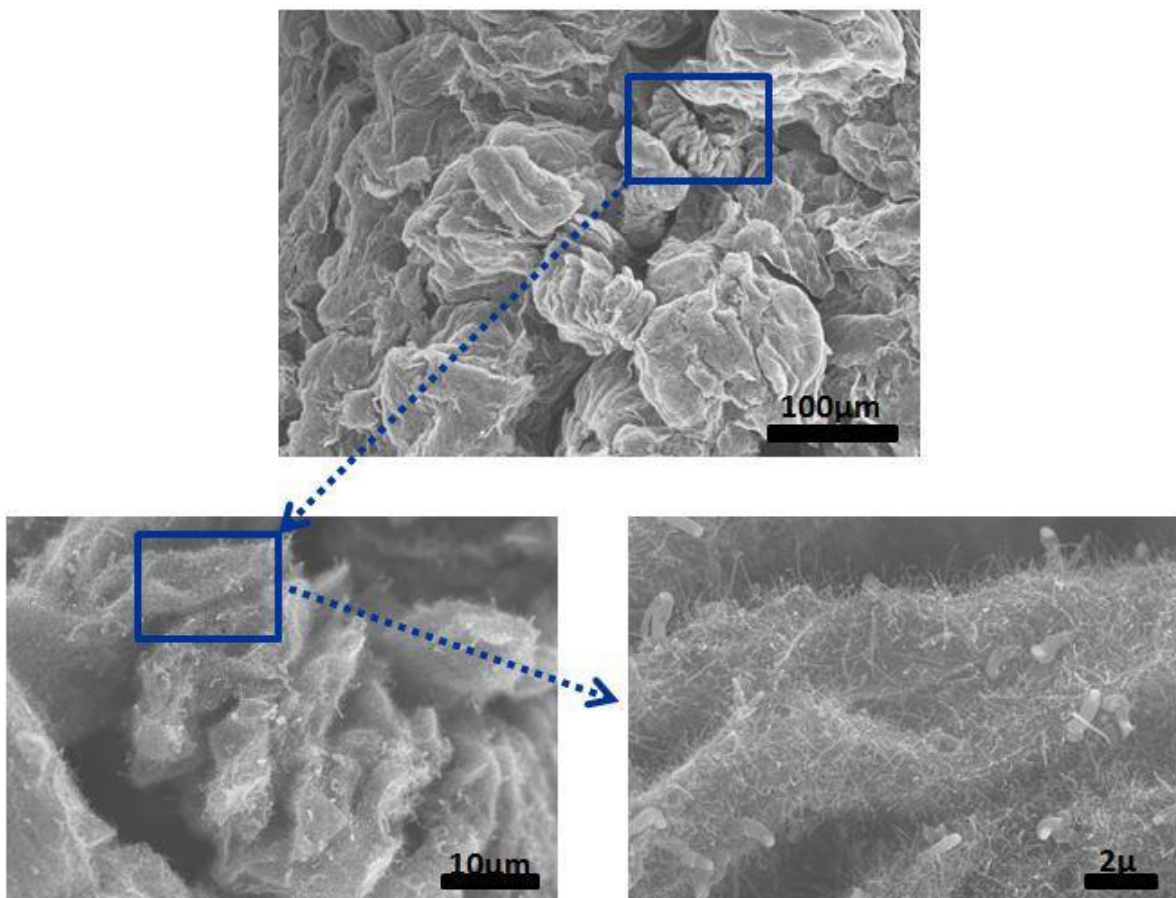


Figure 4.1: SEM images of nitrogen doped carbon nanotubes, confirming the growth of carbon fibers on the surface of the expendable graphite[36]

Figure 4.2 shows the different structures of Fe- and Ni-based NCFs [36]. From the pictures it can be seen that the structures are somewhat different for the Fe- and Ni-NCNFs. The Fe-NCNFs have a smoother surface with clearly defined iron particles in the tip of the carbon nanofibers, whilst the structure of the Ni-NCNFs appears more random.

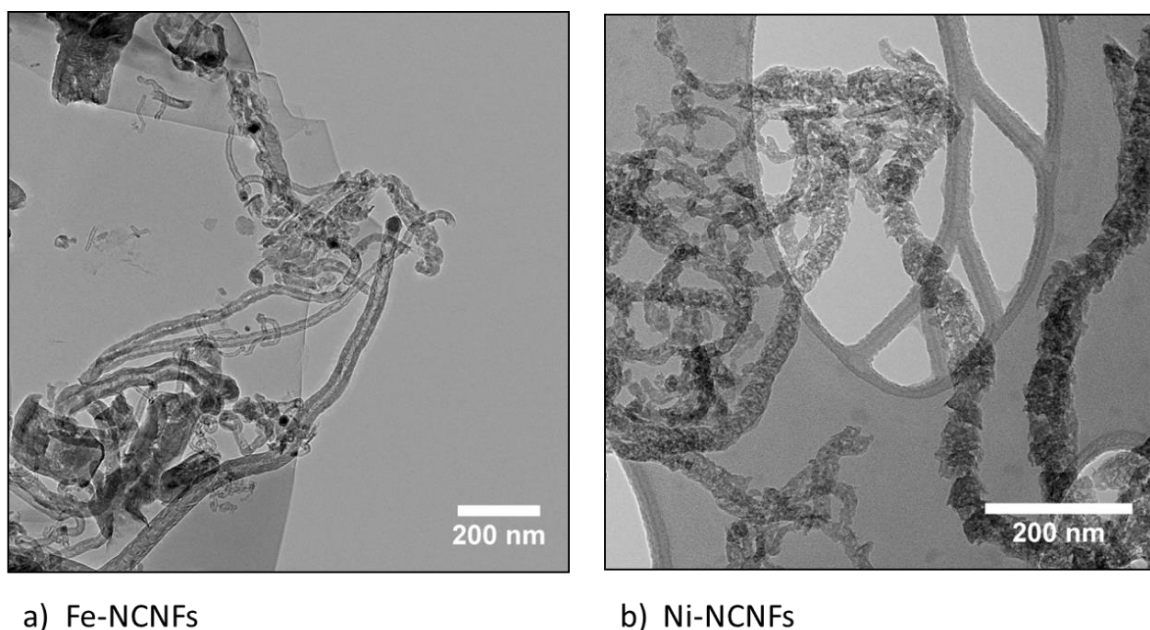
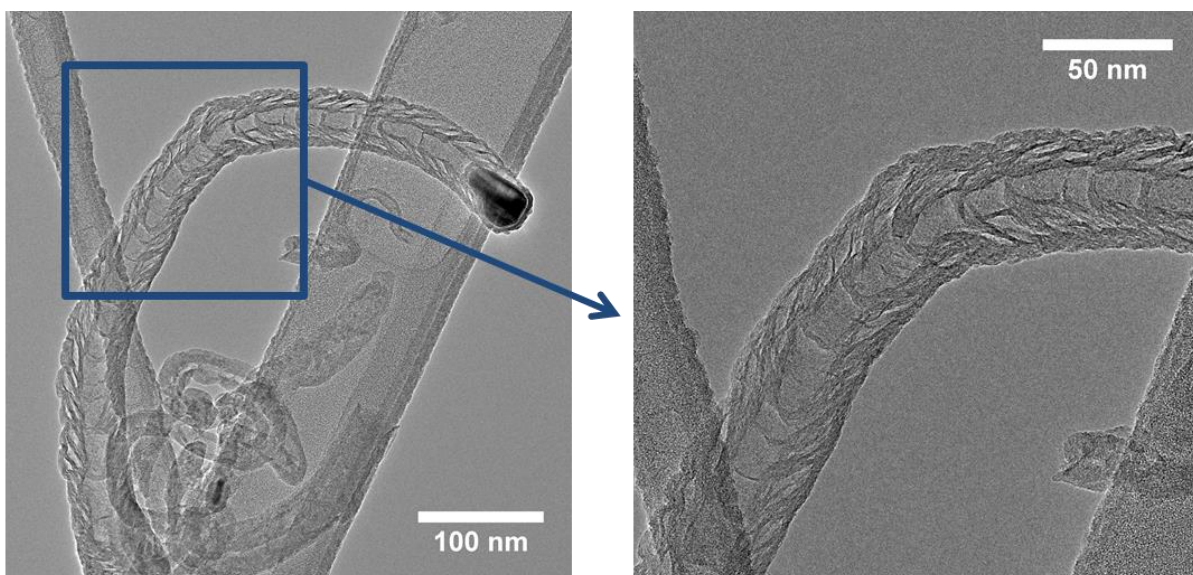


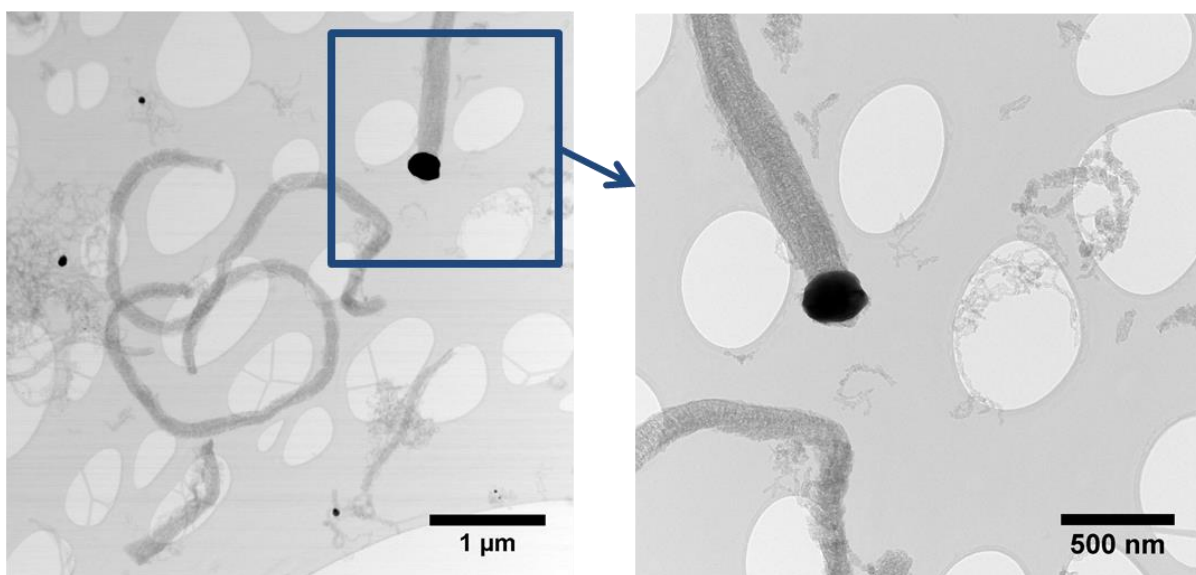
Figure 4.2: The difference in structure for Fe-NCFs (a) and Ni-FCNFs (b). The Fe-NCFs seem to have a smooth bamboo structure, whilst the Ni-NCFs have a more random structure of stacked cups [36].

From Figure 4.2 and 4.3 it can be seen that the carbon nanofibers where iron was used as a growth catalyst have a proper bamboo structure, with periodical closed compartments along the axis of the tube. The nickel based carbon nanofibers however, have a more random structure of stacked cups. For the Ni-NCFs there also are several carbon nanofibers growing on the same nickel particle, which are not seen for the Fe-NCFs.

Figure 4.3 also shows that both the iron and the nickel in the different carbon nanofibers are located at the tip of the carbon fibers. This suggests that both the Fe-NCFs and the Ni-NCFs grows with a tip-growth mechanism, indicating weak interactions between the catalyst and the support. The figure also suggests that the iron particles are smaller and more encapsulated than the nickel particles, whereas the nickel particles are more exposed.



a) Fe-NCNFs



b) Ni-NCNFs

Figure 4.3: Illustration of tip-growth in Fe-NCNFs (a) and Ni-NCNFs (b). The figure also shows the bamboo structure of the Fe-NCNFs, with periodical closed compartments along the tube [36].

4.1.2 BET results

To obtain a trustworthy result, BET were run twice for each sample. The isotherms for the different experiments are shown in Figure 4.4, together with the linear regression lines and formulas.

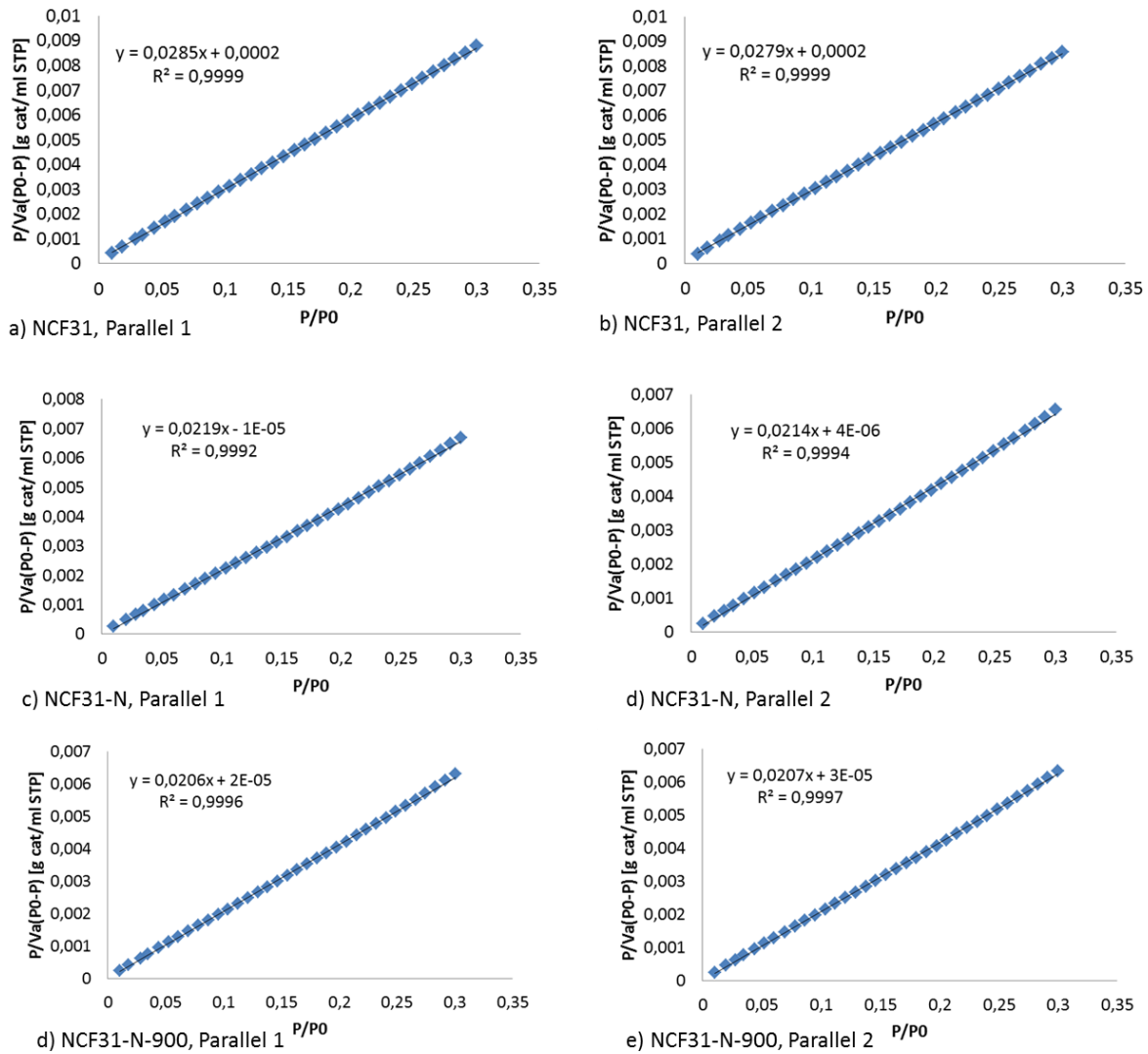


Figure 4.4: Isotherms from the BET analysis of NCF31, NCF31-N and NCF31-N-900, including linear regression lines and formulas.

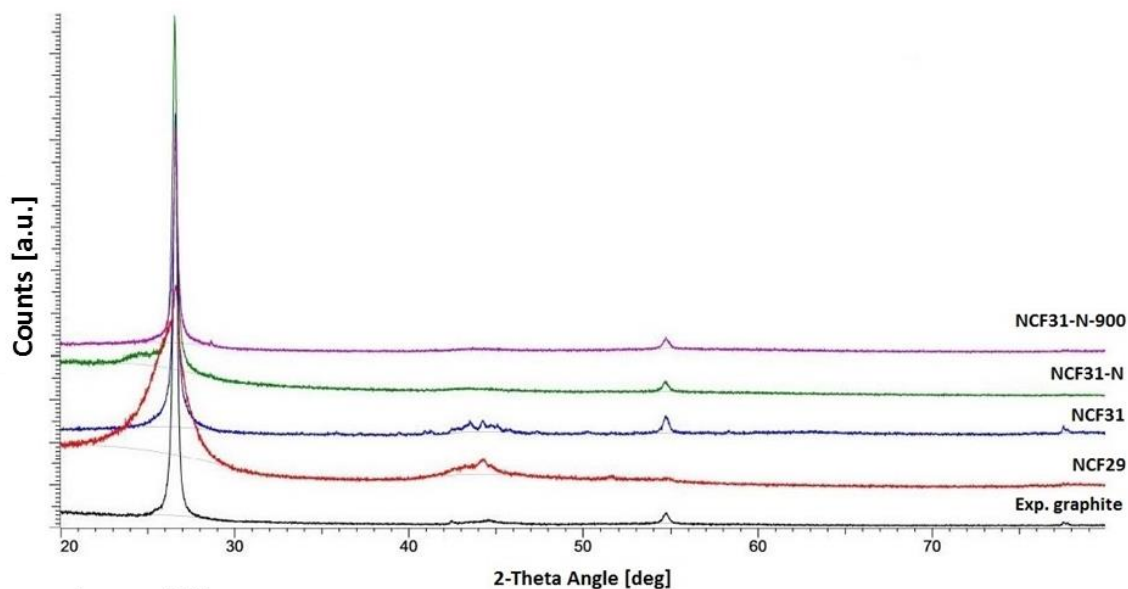
From the BET isotherms and the equations given in the theory, The BET surface area, S_{BET} , of the different samples was calculated. The results are presented in Table 4.1.

Table 4.1: BET surface areas for the samples NCF31, NCF31-N and NCF31-N-900

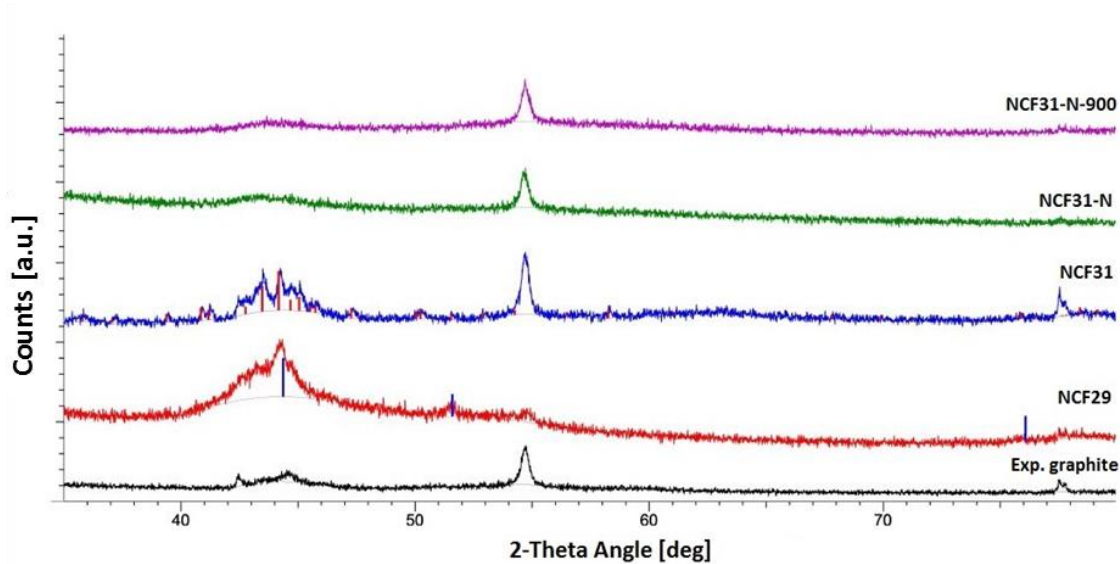
Sample	BET surface area, S_{BET} [m^2/g]		
	<i>Parallel 1</i>	<i>Parallel 2</i>	<i>Average</i>
NCF31	152	155	153,5
NCF31-N	199	203	201
NCF31-N-900	211	210	210,5

4.1.3 XRD results

The results from the XRD-scans for the samples NCF31, NCF31-N, NCF31-N-900 and NCF29 are presented in Figure 4.5. To get a better viewing of the differences between the samples, the figure displays both the original scans (a) and a zoomed version (b).



a) X-ray diffraction scans



b) X-ray diffraction scans, zoomed

Figure 4.5: Original (a) and zoomed (b) X-ray Diffraction scans for XRD scans for NCF31 (blue line), NCF31-N (green line), NCF31-N-900 (purple line), NCF29 (red line) and expandable graphite (black line).

As seen from the figure, it is a distinct difference between the samples. The nickel sample has a broader left peak than the iron samples, and one can clearly see that the several peaks around 44 degrees in sample NCF31 (and NCF29) are reduced with acid treatment (NCF31-N) and annealing (NCF31-N-900). There is also a distinct difference in the peak around 55 degrees, for the nickel and iron samples. The results from the fitting of the Powder Diffraction Files (PDFs) are also shown in the figure, and both confirm that the nickel sample contains nickel, and suggest that the iron in the iron samples is in the form of iron carbide.

4.1.4 X-ray Photoelectron Spectroscopy results

The results from the XPS analysis suggests that there are several forms of nitrogen atoms incorporated in the nitrogen doped carbon nanotubes. As seen in figure 4.6, the as synthesized NCF31 contain pyridinic, quaternary nitrogen groups, as well as pyridinic oxide. It can also be seen that pyrrolic nitrogen groups are introduced after the acid treatment, and then removed again during the annealing process.

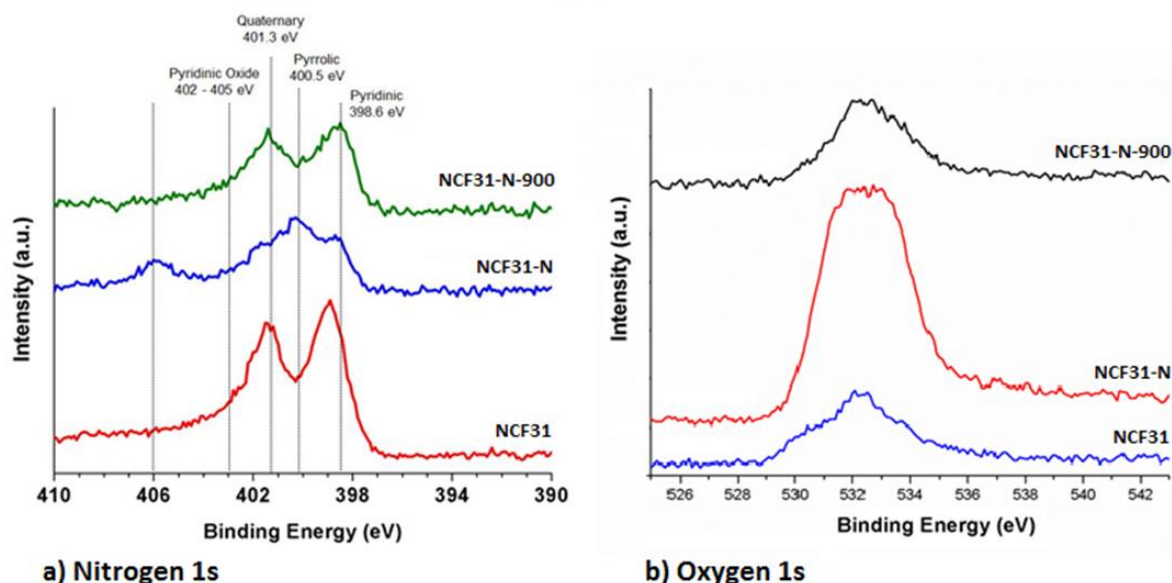


Figure 4.6: XPS scans for NCF31, NCF31-N and NCF31-N-900

The nitrogen/carbon ratio and the oxygen/carbon ratio found from the XPS scans are given in table 4.2.

Table 4.2: Nitrogen/carbon and oxygen/carbon ratios for the samples NCF31, NCF31-N and NCF31-N-900

Catalyst	N/C-ratio (%)	O/C-ratio (%)
NCF31-N-900	2,8	2,8
NCF31-N	2,9	10,8
NCF31	6,6	3,9

4.1.5 TGA results

The results from the TGA results for the samples NCF31 and NCF31-N are presented in Figure 4.7. The black line is the TGA, and the blue line the couples DSC. The figure shows that both the samples undergo a significant drop in mass%, at around 400°C.

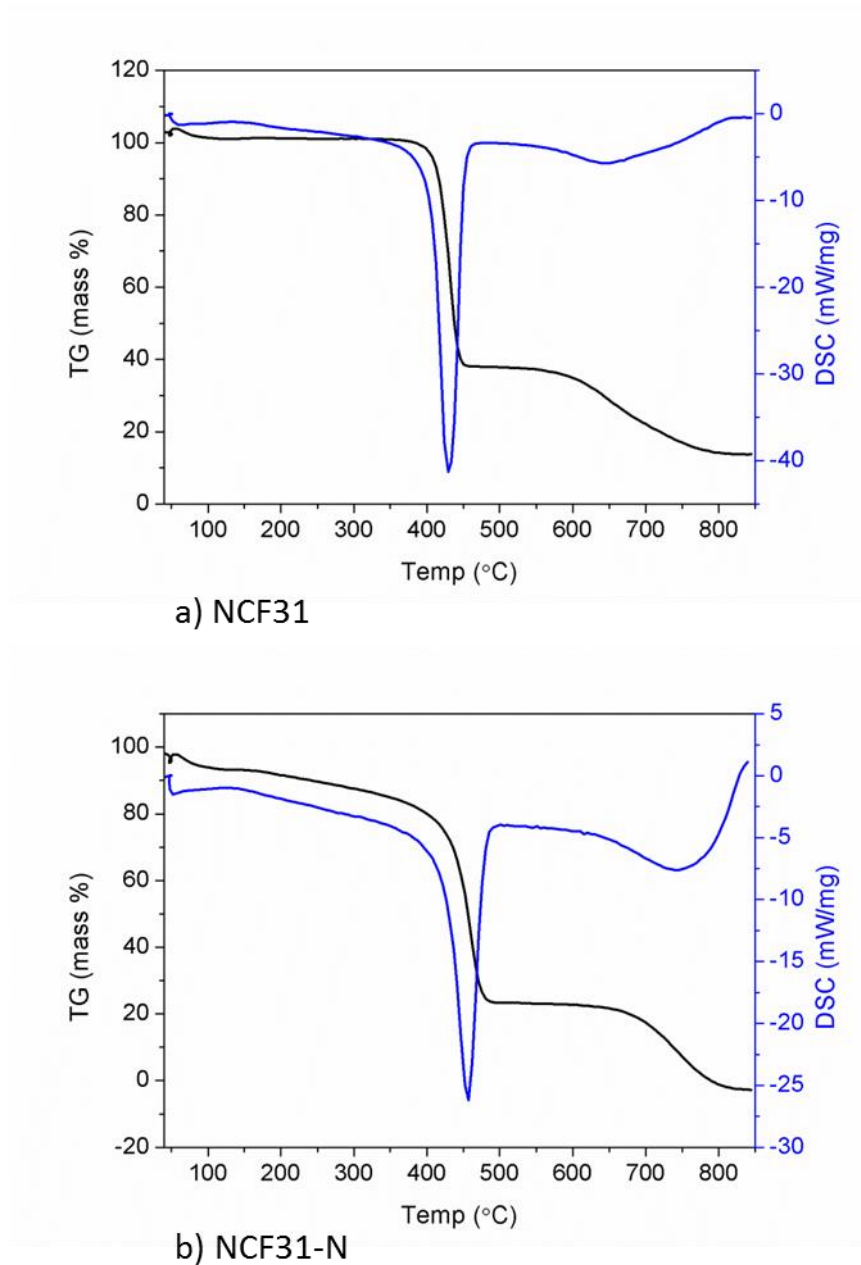


Figure 4.7: TGA results for a) NCF31 and b) NCF31-N. The black line shows the TGA measurements, and the blue line the DSC.

4.3 Oxidative dehydrogenation

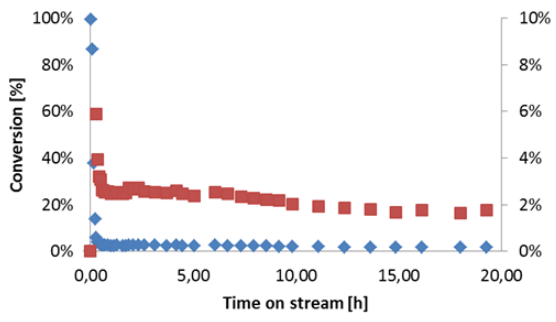
The samples NCF31, NCF31-N, NCF31-N-900 and NCF29 were tested for oxygen dehydrogenation. The raw data for all the samples are given in Appendix D, and the graphs for Vulcan Carbon are presented in Appendix E. The blind test gave a constant conversion of zero, and is thus not presented.

Propene, CO, CO₂ and water were the only detected products from the oxidative dehydrogenation reaction for all the samples. The amount of CO was however too small to perform reasonable calculations, and are therefore not presented here.

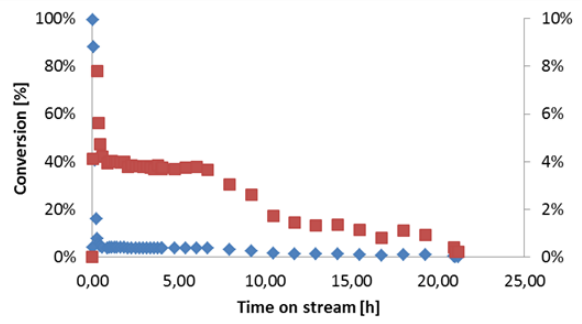
4.3.1 Conversions

The conversions for the different samples are given in Figure 4.7. Since the conversions were generally small, two plots are included for each sample. The blue diamonds represent the full scale plot, whilst the red squares represent the scaled version of the same plot.

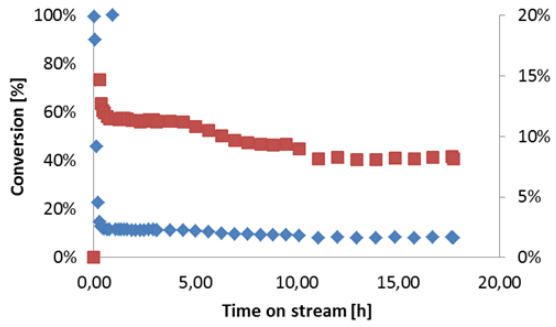
As can be observed from the figure, the nickel based NCF29 shows the best results, with a stable conversion of over 10%. In comparison, the iron based NCF31 have a conversion of around 2%, which in addition seems to be dropping slightly during the last hours of the experiment. The acid treated NCF-N start out marginally better, with a 4% conversion, but then drops drastically after around seven hours on stream. The annealed sample shows the best results of the iron samples, with a conversion that starts out at around 13%, but drops below 10% after about ten hours of running.



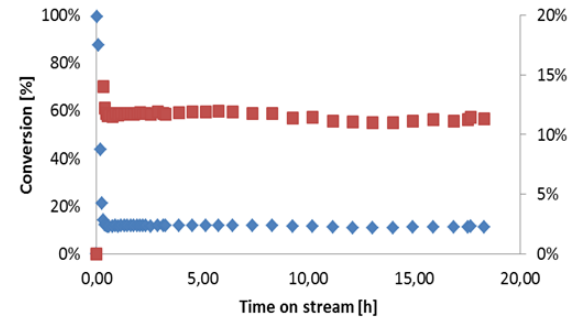
a) NCF31



b) NCF31-N



c) NCF31-N-900



d) NCF29

Figure 4.7: Conversion of propane for a) NCF31, b) NCF31-N, c) NCF31-N-900 and d) NCF29. The blue diamonds represent the full scale plots, and the red squares represent a scaled version of the same plot.

4.3.2 Selectivity for propene

The selectivities for propene for the samples are given in Figure 4.8. As for the conversion, there are two plots for each sample; blue diamonds represent the full scale plot, whereas the red squares represent a scaled version of the same plot. The exception is the plot for NCF31-N, where scaling was determined to be unnecessary due to the large range of the full scale plot.

As observed from the figure, the selectivity for propene is quite unstable in all of the iron samples. NCF31 shows the highest selectivity, and peaks at about 45%. Both the acid treated NCF31-N and the annealed NCF31-N-900 start out with a high selectivity of around 50% and 70% respectively. However, both these samples have a drop in selectivity after about seven hours on stream, and fall below 20% and 5% for NCF31-N and NCF31-N-900 respectively. For the nickel based catalyst the selectivity starts out low, and then increase up to about 15% during the first five hours. The selectivity then seems to drop slightly towards the end of the reaction time.

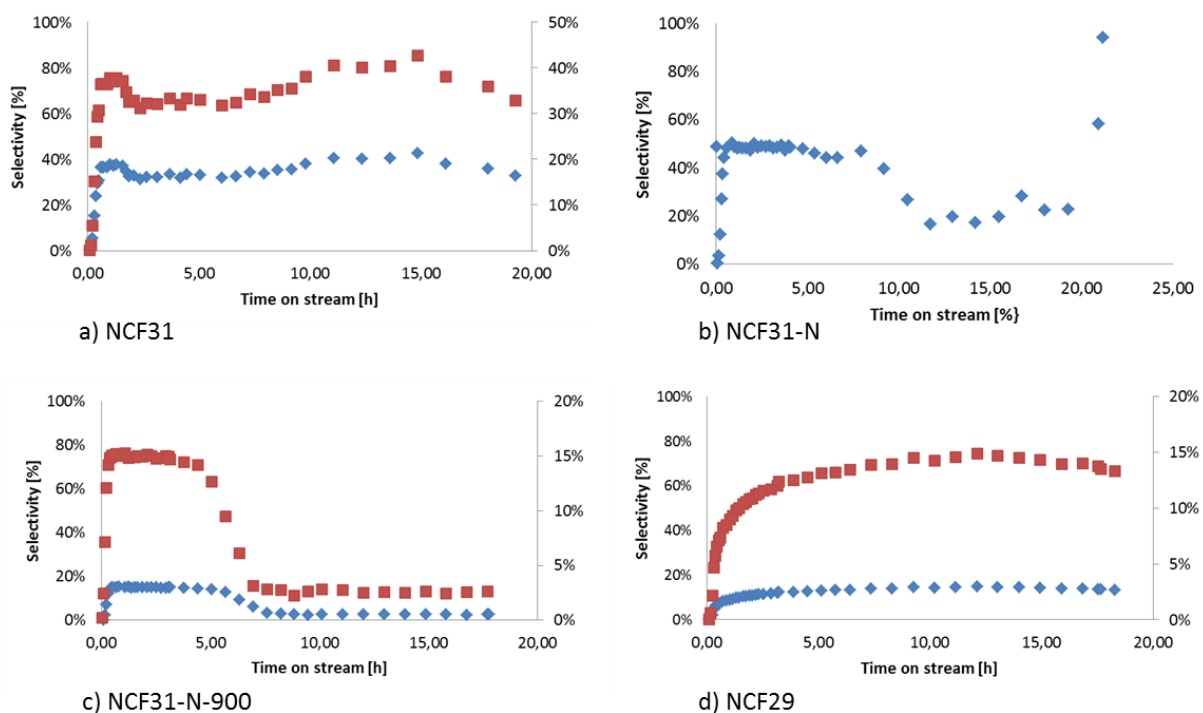


Figure 4.8: Selectivity for propene for a) NCF31, b) NCF31-N, c) NCF31-N-900 and d) NCF29. The blue diamonds represent the full scale plots, and the red squares represent a scaled version of the same plot.

4.3.3 Selectivity for CO₂

The selectivity for CO₂ for the different samples is presented in Figure 4.9. As for the last figures, a scaled version of the plot is given when it was judged to be pertinent. In this case, NCF31-N-900 and NCF29 have both the original plot, and a scaled version.

As seen in the Figure, the iron based NCF31 have a CO₂ selectivity that remains stable at just above 60% for the whole experiment. For NCF31-N and NCF31-N-900 the conversion starts at 60% and around 35% respectively. Then, after around five hours, both samples undergo a sudden drop in selectivity, and stabilize at 20% and 10% respectively. The nickel based NCF29 have a low selectivity from the beginning, but increases steadily up to about 27% during the first 3 hours. After peaking at around 27%, the selectivity decreases steadily for the rest of the experiment and drop below 20% towards the end of the experiment.

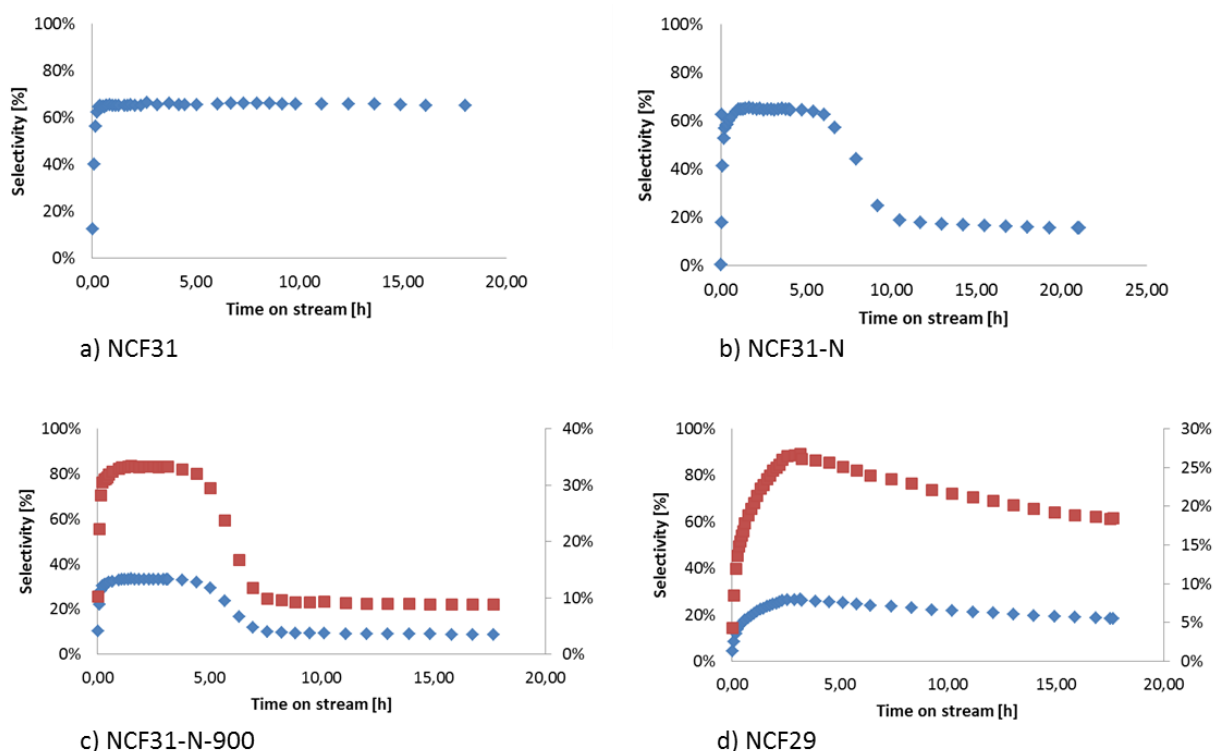


Figure 4.9: Selectivity for CO₂ for a) NCF31, b) NCF31-N, c) NCF31-N-900 and d) NCF29. The blue diamonds represent the full scale plots and the red squares represent a scaled version of the same plot.

4.3.4. Selectivity for H₂O

Figure 4.10 describes the selectivity for H₂O for the four samples. As can be seen from the figure, all of the samples show the opposite trends for the H₂O selectivity as for the CO₂ selectivity. NCF31 have a stable H₂O selectivity just below 40%, whilst the H₂O selectivity for NCF31-N and NCF31-N-900 increase from 40% to 80% and 70% to 90% respectively. The nickel based NCF29 starts with a selectivity at almost 100%, before it becomes more stable at around 80% throughout the experiment.

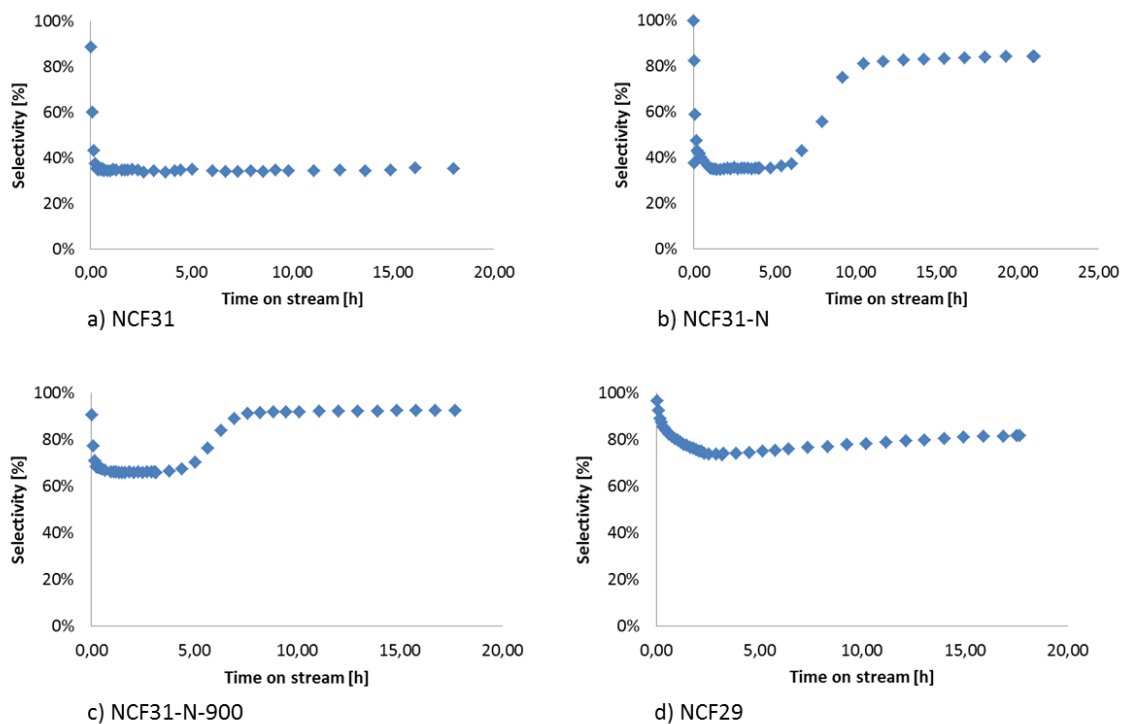


Figure 4.10: Selectivity for H₂O for a) NCF31, b) NCF31-N, c) NCF31-N-900 and d) NCF29.

5. Discussion

5.1 Synthesis

The SEM and TEM pictures confirm that the attempt to grow nitrogen doped carbon nanofibers was successful, and that the carbon fibers grow with a tip growth mechanism. This indicates that the interactions between the support and growth catalyst are weak. The nitrogen and oxygen levels in the samples are confirmed by the XPS, which shows a nitrogen/carbon ratio up to 6.6%.

5.2 Catalyst characterization

5.2.1 BET

The BET surface area determined for the catalysts are displayed in Table 4.1. Several analyses were done on each sample, as the first ones produced unrealistically high surface areas. The reason for this is believed to be the use of too little sample, thus working in the very limits of the operating range of the apparatus. The glass tubes that are used for the BET can only take a certain amount of sample, and when the density is low, one have make an compromise between the maximum volume that should be used, and the actual weight of the sample needed for a stable result. When more sample was used during the analysis, the results became more stable, and for the two parallels given in figure 4.4, the difference between them was less than 3%. This indicates a good reproducibility, though several additional parallels should definitely be conducted before one can be sure of this.

In addition to the difficulties with the amount of sample, the catalyst samples proved very difficult to weigh. Each sample was weighed twice to get as accurate results as possible, but there still are uncertainties about the measurements. As well as being extremely static and thus difficult to work with in all stages of this project, the samples do not have a completely homogeneous composition. The particle size varies in the sample, and if different analysis was performed on different particle sized, this could have a substantial effect on the results.

The adsorption/desorption isotherms are given in Appendix F. All the isotherms are quite similar, and resembles “type 2” isotherms, which are known to be suitable for BET isotherms [9, 23]. The figure shows that the isotherms have a slight desorption hysteresis for high pressures, but this effect occurs well outside the area used for the BET plots, and the measurements can therefore be assumed to be accurate.

5.2.2 XRD

The XRD results are shown in Figure 4.5. As seen from the figure, the amount of iron decreases drastically after acid treatment, and also seems to decrease a bit further after the annealing. This shows that the effort to remove iron from the NCF31 sample by treating it with nitric acid was successful. The peak is not completely removed however, which most likely mean that it is still some iron left in the sample after the treatment. The Powder Diffraction Files suggest that the iron in the samples is in the form of monoclinic iron carbide. It is also confirmed by the Powder Diffraction Files that there is nickel in the nickel based sample, but here no nickel carbide was detected, only pure nickel.

5.3 Activity measurements

The only products detected by the GC where propene, CO, CO₂ and water. The amount of CO however, was so small that further calculations proved difficult, giving close to zero and even negative selectivities for all of the samples. The results from the calculations on CO are consequently not given.

During the experiment, two of the peaks from the GC proved difficult to identify. These peaks where found in column one and two, at retention time 1,44 and 1,63 respectively. The peak in column one were not very far from the retention time one would expect to find methane, but if the methane peak where to shift that much towards either side, the peaks for the other components should shift accordingly. As this did not happen, the most likely conclusion is that methane is not one of the products.

As for the unidentified peaks in column two, a small double peak at retention times 1,5 and 1,6 shows up in every single measurement, for every gas, including the calibration gases. This leads to the conclusion that this is a systematic error from the GC. However, the peak at 1,6 grew considerably bigger during the reaction for the catalyts. Neither the blank test nor the sample of Vulcan carbon showed this increase in size, suggesting that the peak is a product of the oxidative dehydrogenation reaction, and not only a contamination of some kind. However, during the calibrations (see appendix C), all the expected products where located, without the 1,6 peak showing up. This suggests that the peak is neither CH₄, C₂H₆, C₂H₄, C₃H₆, CO nor CO₂.

From Figure 7 one can see that in general, the conversion for all the samples is low. NCF31 and NCF31-N both have a lower conversion than the Vulcan Carbon (see Appendix E), and the NCF31-N-900 and NCF29 are only slightly higher.

For calculation of the selectivities, both the carbon balance and the oxygen balance were used. When using the oxygen balance, the sum of the products containing oxygen was very close to 100% for all the samples, indicating that the calculations are fairly accurate. When using the carbon balance to calculate the selectivity for CO₂ however, some of the samples show questionable results. For NCF31, the CO₂ selectivity alone reaches a percentage of over a hundred, whereas for the other samples the percentages for propane and CO₂ selectivity either adds up to more than a hundred, or considerably less (10-40%). This indicates some uncertainties in the carbon balance, and consequently the oxygen balance where used to calculate the CO₂ selectivities in the end. This means that the selectivities for propane are uncertain, and the low percentage could indicate that there are some products containing carbon that haven't been found. It is possible that this could be the unknown compound in column two, as the high retention time indicates a heavy product, possibly one containing carbon.

The mass flow controllers also contribute to some uncertainties. Even though the MFC was calibrated last year, the flow calculated from the calibration graphs does not altogether match the actual flows. This is most likely due to the low flows used in this experiment (total flow of 33,3 ml/min), and the fact that the MFCs are not perfectly suitable for such small flows. The flow is believed to be stable even though it might not be stable at the correct flow, so it is reasonable to believe that since the change in the composition of the gas flow was not very big, the effects on the results are minimal.

The fact that no CH₄ was detected means that no cracking of propane occurred during the experiment. This is reasonable, as the temperature of the experiment was set at 400°C, and problems regarding cracking are usually reported at higher temperatures [37, 38]

The nickel based catalyst had a better conversion than all of the iron based samples. The annealed NCF31-N-900 started out at the same conversion, just above ten percent, but decreased steadily the first 10 hours, before it stabilized at around eight percent. Although the selectivity for propene was better for NCF31 than for NCF29, the iron based sample also had a significantly higher selectivity for CO₂ than the nickel sample.

The difference in performance might be caused by the difference in structure for the two types of carbon nanofibers. Where the iron based NCFs showed a smooth bamboo structure, the nickel based NCFs showed a more random structure of "stacked cups." Since the bamboo like structure don't have any edges between the edges of the nanotube itself, it will contain more

quarternary groups, since these are incorporated in the middle of the carbon structure. The three other nitrogen groups, pyridinic, pyrrolic and pyridinic oxide, are more often located on the edges, and are thus more important in the stacked cups structure, which have edges on each “cup” all along the carbon nanotube. If the different nitrogen and oxygen groups play different roles in the ODH reaction, the different structures will matter greatly. For un-doped carbon nanofibers, the herringbone structure is reported to have higher activity and selectivity towards propene than tubular carbon nanofibers [37], thus suggesting that the edges contain more active groups for the oxidative dehydrogenation reaction than the basal planes of the carbon structure.

Another possible explanation for the difference in activity is the difference in the metal particles in the NCFs. Though the aim is to remove all of the metal from the growth catalyst, some of the metal will most likely still be in the sample after the treatment. Since the iron particles seemed to be more encapsulated than the nickel particles, it could be that the nickel that might be left in the sample is more likely to contribute to the reaction.

As mentioned in the theory, a correlation between the oxygen reduction reaction and oxidative dehydrogenation has been found. It is also generally accepted that either quarternary or pyridinic nitrogen groups are responsible for the catalytic activity of nitrogen doped CNFs in the oxygen reduction reaction [39, 40]. If this is correct, then it could be that the pyridinic nitrogen groups, which are found on the edge planes, are some of the reason why the nickel based samples had a higher reaction than the iron based ones, which in theory should contain less pyridinic groups because of the bamboo structure.

The selectivities for propene reached from 15% for the nickel based sample NCF29, to almost 80% for the iron based NCF31. However, both sample NCF31-N and sample NCF31-N-900 had a drop in selectivity after 7-10 hours. This could be due to propane adsorption on the reduced catalyst, which has been suggested to be detrimental for alkene selectivity. According to Frank et al [15], this problem could be reduced by introducing boron oxide to the CNFs.

6. Conclusions and future work

6.1 Synthesis and characterizations

The SEM and TEM pictures confirm that the goal of making nitrogen doped carbon nanofibers through CVD was successful. This was also further confirmed with the XPS.

The XRD confirmed that the acid treatments did indeed remove most of the iron in the samples. It is likely that some of the iron is still left in the sample, but hopefully this is encapsulated in the carbon (and thus not reached by the acid), and will not contribute to the surface reactions.

To determine the surface area of the samples, BET was used. It was discovered that too small amounts of sample gave unstable results, but when the sample weight was close to 80 mg, the test results became consistent over several parallels. This could be due to the operating limits of the apparatus, but it could also be that the sample particles were about the same size for the last parallels, and not for the unstable ones, since the samples weren't completely homogeneous in particle size. In addition to the difficulties with sample mass, the weighing of the samples proved difficult. To prevent errors each weighing was performed several times, and the measurements are therefore believed to be fairly accurate. The BET isotherms are all of Type II, making them suitable for BET analysis, and the area used for calculations was shown to be linear. Thus it can be assumed that the calculations for BET surface area were fairly accurate.

6.2 Activity and selectivity measurements

From the activity measurements, it seems like the nickel based samples are best when it comes to activity alone. It also produces less CO₂. On the other hand, the iron based samples have a higher selectivity towards propene, according to the measurements. The difference is believed to be due to the difference in structure between the two types of carbon nanofibers, as the difference in edge vs basal planes, and thus different nitrogen groups, are assumed to be high. The selectivity for propane was high in the iron samples, but showed a drop after 7-15 hours in both the acid treated NCF31-N and the annealed NCF31-N-900. This could be due to propane adsorption on the reduced catalyst, which has been suggested to be detrimental for alkene selectivity.

6.3 Further work

It would be useful to perform further testing with both varying temperature and flow, to see if the different parameters have an effect on the selectivities. It would of course also be of interest to run more than one parallel for each set of parameters, to see if the results are reproducible. It would also be of great interest to introduce different doping agents in the carbon nanofibers, such as boron and phosphorous, and compare the activity and selectivity of the nitrogen doped CNFs.



7. References

1. Radstake, P.B., *Oxygen Assisted Dehydrogenation of Ethane over Alumina Supported Pt-Sn Catalysts*, in *Department of Chemical Engineering*. 2012, PhD Thesis, Norwegian University of Science and Technology.
2. Bricker, J.c., *Advanced Catalytic Dehydrogenation Technologies for Production of Olefins*. 2012.
3. Gorelkin, Y.V., *Concepts and models of the catalytic dehydrogenation of propane*, in *Department of Chemical Engineering*. 2013, PhD Thesis, Norwegian University of Science and Technology.
4. Yu, D., et al., *Metal-Free Carbon Nanomaterials Become More Active than Metal Catalysts and Last Longer*. *The Journal of Physical Chemistry Letters*, 2010. **1**(14): p. 2165-2173.
5. Chizari, K., et al., *Nitrogen-Doped Carbon Nanotubes as a Highly Active Metal-Free Catalyst for Selective Oxidation*. *ChemSusChem*, 2012. **5**(1): p. 102-108.
6. Cao, Y., et al., *Nitrogen-, phosphorous- and boron-doped carbon nanotubes as catalysts for the aerobic oxidation of cyclohexane*. *Carbon*, 2013. **57**(0): p. 433-442.
7. Maciel, I.O., et al., *Synthesis, Electronic Structure, and Raman Scattering of Phosphorus-Doped Single-Wall Carbon Nanotubes*. *Nano Letters*, 2009. **9**(6): p. 2267-2272.
8. Chen, C., et al., *Revealing the enhanced catalytic activity of nitrogen-doped carbon nanotubes for oxidative dehydrogenation of propane*. *Chemical Communications*, 2013. **49**(74): p. 8151-8153.
9. Niemantsverdriet, I.C.J.W., *Concepts of Modern Catalysis and Kinetics*. 2 ed. 2007.
10. Morgan, P., *History and Early Development of Carbon Fibers*, in *Carbon Fibers and Their Composites*. 2005, CRC Press. p. 65-120.
11. Springer, *Handbook of Nanomaterials*. 2013: Springer.
12. Biddinger, E., D. von Deak, and U. Ozkan, *Nitrogen-Containing Carbon Nanostructures as Oxygen-Reduction Catalysts*. *Topics in Catalysis*, 2009. **52**(11): p. 1566-1574.
13. Atkins, P., et al., *Shriver and Atkins' Inorganic Chemistry*. 2010: Oxford University Press.
14. Cavani, F. and F. Trifirò, *The oxidative dehydrogenation of ethane and propane as an alternative way for the production of light olefins*. *Catalysis Today*, 1995. **24**(3): p. 307-313.
15. Frank, B., et al., *Heteroatoms Increase the Selectivity in Oxidative Dehydrogenation Reactions on Nanocarbons*. *Angewandte Chemie International Edition*, 2009. **48**(37): p. 6913-6917.
16. Sui, Z.-j., et al., *Oxidative dehydrogenation of propane over catalysts based on carbon nanofibers*. *Catalysis Today*, 2005. **106**(1-4): p. 90-94.
17. Matthew, P.W., et al., *Correlation Between Oxygen Reduction Reaction and Oxidative Dehydrogenation Activities Over Nanostructured Carbon Catalysts*. *Catalysis Letters*, 2010.
18. Siahvashi, A., D. Chesterfield, and A.A. Adesina, *Nonoxidative and Oxidative Propane Dehydrogenation over Bimetallic Mo-Ni/Al₂O₃ Catalyst*. *Industrial & Engineering Chemistry Research*, 2013. **52**(11): p. 4017-4026.
19. Barsan, M.M. and F.C. Thyron, *Kinetic study of oxidative dehydrogenation of propane over Ni-Co molybdate catalyst*. *Catalysis Today*, 2003. **81**(2): p. 159-170.
20. J.R. Creighton, P.H., *Introduction to Chemical Vapor Deposition (CVD)*.
21. Magrez, A., et al., *Catalytic CVD Synthesis of Carbon Nanotubes: Towards High Yield and Low Temperature Growth*. *Materials*, 2010. **3**(11): p. 4871-4891.
22. Che, M. and J.C. Vedrine, *Characterization of Solid Materials and Heterogeneous Catalysts: From Structure to Surface Reactivity*. 2012: Wiley.
23. Mørk, P.C., *Overflate og Kolloidkjemi, Grunnleggende Prinsipper og Teorier*. 8 ed. 2004, Trondheim : Norges teknisk-naturvitenskapelige universitet, Institutt for kjemisk prosesssteknologi, 1999.

24. Omid, M., *Thermodynamics of Interfaces*. Thermodynamics - Interaction Studies - Solids, Liquids and Gases. 2011.
25. Singh, K.S.W., et al., *Characterization of Solid Catalysts: Sections 3.1.1 – 3.1.3*, in *Handbook of Heterogeneous Catalysis*. 2008, Wiley-VCH Verlag GmbH. p. 427-582.
26. Cockcroft, J.K. *Instrument X-ray Optics - Reflection Geometry*. Available from: <http://pd.chem.ucl.ac.uk/pdnn/inst1/optics1.htm>.
27. Askeland, D., P. Fulay, and W. Wright, *The Science and Engineering of Materials*. 2010: Cengage Learning.
28. *The International Centre for Diffraction Data (ICDD)*. Available from: <http://www.icdd.com/>.
29. Mabena, L., et al., *Nitrogen-doped carbon nanotubes as a metal catalyst support*. *Applied Nanoscience*, 2011. **1**(2): p. 67-77.
30. van Dommele, S., et al., *Tuning nitrogen functionalities in catalytically grown nitrogen-containing carbon nanotubes*. *Carbon*, 2008. **46**(1): p. 138-148.
31. PerkinElmer. *Thermogravimetric Analysis (TGA) - A Beginner's Guide*. [cited 2014 11.06.2014]; Available from: http://www.perkinelmer.com/cmsresources/images/44-74556gde_tgabeginnersguide.pdf.
32. Pyramides, G., J.W. Robinson, and S. William Zito, *The combined use of DSC and TGA for the thermal analysis of atenolol tablets*. *Journal of Pharmaceutical and Biomedical Analysis*, 1995. **13**(2): p. 103-110.
33. McNair, H.M.M., James M. , *Basic Gas Chromatography*. 2 ed. 2009, Hoboken, NJ, USA Wiley-Interscience
34. Grob, R.L. and E.F. Barry, *Modern Practice of Gas Chromatography*. 2004: Wiley. 1064.
35. A. Braithwaite, F.J.S., *Chromatographic Methods*. 5 ed. 1996: Blackie academic & Professional.
36. Buan, M.E.M., *In Preparation*. PhD Thesis, Norwegian University of Science and Technology.
37. Chen, D., et al., *Carbon mediated catalysis: A review on oxidative dehydrogenation*. *Chinese Journal of Catalysis*, 2014. **35**(6): p. 824-841.
38. Weckhuysen, B.M. and R.A. Schoonheydt, *Alkane dehydrogenation over supported chromium oxide catalysts*. *Catalysis Today*, 1999. **51**(2): p. 223-232.
39. Maldonado, S. and K.J. Stevenson, *Influence of Nitrogen Doping on Oxygen Reduction Electrocatalysis at Carbon Nanofiber Electrodes*. *The Journal of Physical Chemistry B*, 2005. **109**(10): p. 4707-4716.
40. Kundu, S., et al., *The formation of nitrogen-containing functional groups on carbon nanotube surfaces: a quantitative XPS and TPD study*. *Physical Chemistry Chemical Physics*, 2010. **12**(17): p. 4351-4359.

Appendix A – Risk assessments

The risk assessments for the project are given in figure A.1 to A5.

NTNU  HSE	Hazardous activity identification process			
Unit: <i>Institutt for kjemisk prosess teknologi</i> Line manager: Edd Blekkan		Prepared by HSE section Approved by The Rector	Number HMSRV-2601	Date 09.01.2013 Replaces 01.12.2008
Date: 18.06.2014				
Participants in the identification process (including their function): Magnus Rønning (Supervisor), Kaia Andersson Jensen (Student)				
Short description of the main activity/main process: Master project for Kaia Andersson Jensen. Doped carbon nanostructures as metal-free catalysts for oxidative dehydrogenation of light alkanes.				
Is the project work purely theoretical? (YES/NO): No <i>Answer "YES" implies that supervisor is assured that no activities requiring risk assessment are involved in the work. If YES, briefly describe the activities below. The risk assessment form need not be filled out.</i>				
Signatures: <i>Magnus Rønning</i>		Responsible supervisor: <i>Magnus Rønning</i>		
Signatures: <i>Kaia A. Jensen</i>		Student: <i>Kaia A. Jensen</i>		

ID nr.	Activity/process	Responsible person	Existing documentation	Existing safety measures	Laws, regulations etc.	Comment
1	Use of flammable gas	Magnus Rønning/ Kaia Jensen	Laboratory handbook, safety data sheets	Gas detectors and alarms	NEK 420, regulations concerning use in hazardous areas	
2	Use of electric furnace	Magnus Rønning/ Kaia Jensen	Laboratory handbook, instruction book for the furnace	Grounding system for electricity	Regulations inspection of electrical installations and electrical equipment	
3	Handling of carbon nanomaterials	Magnus Rønning/ Kaia Jensen	Safety data sheets	Fume hoods, safety goggles, face masks, gloves		
4	Handling of corrosive chemicals	Navaneethan Muthuswamy/ Kaia Jensen	Safety data sheets	Fume hoods, safety goggles, gloves		
5	Heating of flammable liquids	Navaneethan Muthuswamy/ Kaia Jensen	Safety data sheets	Fume hoods, safety goggles, gloves		
6	BET analysis	Karin Dragsten/ Kaia Jensen	Written instructions, Safety data sheets, apparatus card	Gassdetektorsystem, berbare gassdetektorer, advarselskilt	the Working Environment Act	
7	TGA analysis	Karin Dragsten/ Kaia Jensen	Written instructions, Safety data sheets, apparatus card	Gassdetektorsystem, berbare gassdetektorer, advarselskilt	the Working Environment Act	
8	XRD analysis	Julian R Tolchard/ Kaia Jensen		safety goggles, gloves	the Working Environment Act	Operated by apparatus responsible

Figure A.1: Risk assessment, part 1

NTNU		Prepared by		Number		Date	
		HSE section		HMSRV2803E		04.02.2011	
HSE/KS		Approved by				Replaces	
		The Rector				01.12.2006	

Risk assessment

Unit: (Department)
 Line manager:
 Participants in the identification process (including their function):
 Short description of the main activity/main process: Master project for student xx. Project title.
 Signatures: Responsible supervisor: *Margaret M* Student: *Kaia A Jansen*

Date:

ID.	Activity from the identification process	Potential undesirable incident/strain	Likelihood:			Consequence:			Risk Value (human)	Comments/status Suggested measures
			Likelihood (1-5)	Human (A-E)	Environment (A-E)	Economy/Material (A-E)	Material (A-E)			
1	Use of flammable gas	Small gas leak	2	A	A	A	A	A2	Perform leak tests. Gas detectors and foam leak test should be readily available	
1	Use of flammable gas	Large gas leak	1	C	B	B	B	C1	Operators of the rig should have adequate training in the use of gases under high pressure	
2	Use of electric furnace	Electric shock	1	C	A	A	B	C1	Monitoring the quality of the electrical insulation. Avoid contact with uninsulated parts.	
2	Use of electric furnace	Uncontrolled heating	1	C	B	B	C	C1	Operators of the rig should have adequate training in the use of the thermocouple and the control box.	
2	Use of electric furnace	Burn injuries	1	C	A	A	A	C1	Careful work will minimize the risk of burns. Lab coat and goggles should be worn.	
2	Use of electric furnace	Fire	1	C	C	C	D	C2	Careful work will minimize the risk of fire.	
3	Handling of carbon nanomaterials	Inhalation	2	C	A	A	A	C2	Great uncertainty about the hazards concerning carbon nanomaterials. Precautionary actions should be taken.	
4	Handling of corrosive materials	Skin contact	2	D				D2	Careful work will minimize the risk of injury. Lab coat and goggles should be worn.	
4	Handling of corrosive materials	Eye contact	1	D				D1	Careful work will minimize the risk of injury. Lab coat and goggles should be worn.	
5	Heating of flammable liquids	Flammable/potential explosive gas formation	1	C	A	A	B	C1	Use of fume hoods, cooling water	
6	Sample handling	Sample drawn into apparatus by vacuum	2				B		Adequate training in use of the apparatus	

Figure A.2: Risk assessment, part 2

NTNU		Risk assessment		Prepared by	Number	Date
				HSE section	HMSRV2603E	04.02.2011
				Approved by		Replaces
				The Rector		01.12.2006

6	Handling of liquid nitrogen	2	D	D2	Careful work will minimize the risk of injury. Lab coat and goggles should be worn.		
6	Handling of liquid nitrogen	1	D	D1	Careful work will minimize the risk of injury. Lab coat and goggles should be worn.		
7	Heating og sample	2	B	B2	Careful work will minimize the risk of injury. Lab coat and goggles should be worn.		
8	Sample preparation	2	C	C2	Great uncertainty about the hazards concerning carbon nanomaterials. Precautionary actions should be taken		

Likelihood, e.g.:
 1. Minimal
 2. Low
 3. Medium
 4. High
 5. Very high

Consequence, e.g.:
 A. Safe
 B. Relatively safe
 C. Dangerous
 D. Critical
 E. Very critical

Risk value (each one to be estimated separately):
 Human = Likelihood x Human Consequence
 Environmental = Likelihood x Environmental consequence
 Financial/material = Likelihood x Consequence for Economy/material

Potential undesirable incident/strain

Identify possible incidents and conditions that may lead to situations that pose a hazard to people, the environment and any materiel/equipment involved.

Criteria for the assessment of likelihood and consequence in relation to fieldwork

Each activity is assessed according to a worst-case scenario. Likelihood and consequence are to be assessed separately for each potential undesirable incident. Before starting on the quantification, the participants should agree what they understand by the assessment criteria:

Likelihood	Low 2	Medium 3	High 4	Very high 5
Minimal 1	Once every 10 years or less	Once a year or less	Once a month or less	Once a week

Consequence	Human	Environment	Financial/material
Grading			
E Very critical	May produce fatality/ies	Very prolonged, non-reversible damage	Shutdown of work > 1 year.
D Critical	Permanent injury, may produce serious health damage/sickness	Prolonged damage. Long recovery time.	Shutdown of work 0.5-1 year.

Figure A.3: Risk assessment, part 3

NTNU	Risk assessment			Prepared by	Number	Date
				HSE section	HMSRV2603E	04.02.2011
HSE/IKS				Approved by		Replaces
		The Rector		01.12.2006		



C Dangerous	Serious personal injury	Minor damage. Long recovery time	Shutdown of work < 1 month
B Relatively safe	Injury that requires medical treatment	Minor damage. Short recovery time	Shutdown of work < 1 week
A Safe	Injury that requires first aid	Insignificant damage. Short recovery time	Shutdown of work < 1 day

The unit makes its own decision as to whether opting to fill in or not consequences for economy/materiel, for example if the unit is going to use particularly valuable equipment. It is up to the individual unit to choose the assessment criteria for this column.

Risk = Likelihood x Consequence

Please calculate the risk value for "Human", "Environment" and, if chosen, "Economy/materiel", separately.

About the column "Comments/status, suggested preventative and corrective measures":

Measures can impact on both likelihood and consequences. Prioritise measures that can prevent the incident from occurring; in other words, likelihood-reducing measures are to be prioritised above greater emergency preparedness, i.e. consequence-reducing measures.

Figure A.4: Risk assessment, part 4

NTNU		Risk matrix		Number	Date
	HSE/KS	prepared by HSE Section		HMSRV2604	8 March 2010
		approved by Rector		Page	Replaces
				4 of 4	9 February 2010
					

MATRIX FOR RISK ASSESSMENTS at NTNU

CONSEQUENCE		E1	E2	E3	E4	E5
Extremely serious		D1	D2	D3	D4	D5
Serious		C1	C2	C3	C4	C5
Moderate		B1	B2	B3	B4	B5
Minor		A1	A2	A3	A4	A5
Not significant		Very low	Low	Medium	High	Very high
		LIKELIHOOD				

Principle for acceptance criteria. Explanation of the colours used in the risk matrix.


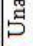
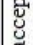
Colour	Description
	Unacceptable risk. Measures must be taken to reduce the risk.
	Assessment range. Measures must be considered.
	Acceptable risk. Measures can be considered based on other considerations.

Figure A.5: Risk assessment, part 5

Appendix B – Raw data from the gas chromatograph

The raw data (areas) from the GC for NCF31, NCF31-N, NCF31-N-900 and NCF29 are given in Table B.1-B.4.

Table B.1: Raw data from the gas chromatograph for parallel 1, NCF31

time on stream [h]	A He [uV*s]	A H2 [uV*s]	A O2 [uV*s]	A N2 [uV*s]	A ? [uV*s]	A CO [uV*s]	A CO2 [uV*s]	A ? [uV*s]	A C3H8 [uV*s]	A C3H6 [uV*s]
0,00			2647	51001			0		56429	0
0,01			19	71741					251	
0,08			15	69177		15	6355		7448	35
0,15	50	464	13	59119	534	53	16435	247438	34999	253
0,22	29	521	12	54027	538	71	22383	2721	48547	421
0,29	17	526	7	52171	478	74	24574	3686	53112	494
0,37	14	529	8	51686	520	67	25393	4351	54207	516
0,44		488	7	51511	506	64	25629	4786	54619	521
0,51		518		51374	476	63	25408	5032	54688	524
0,58		492		51271	501	74	25595	5282	54945	529
0,65		515		51182	477	67	25505	5400	54961	526
0,72		512	9	51170	493	72	25670	5547	54996	514
0,87		505	13	51126	485	64	25596	5687	54986	515
1,01		509	8	51108	474	62	25752	5805	55025	519
1,15		510	7	51152	508	73	25704	5817	55034	506
1,29		509	7	51180	515	63	25598	5827	55006	525
1,57		502	8	51149	509	64	25636	6054	55039	507
1,72		498	9	51136	514	62	25599	6112	55019	481
1,86		494	11	51129	518	63	25560	6152	54898	488
2,07		475	4	51098	508	57	25779	6104	54930	483
2,35		479	4	51113	588	59	25637	6149	54883	472
2,64		479	7	51079	471	53	25683	6247	54975	461
3,14		468	5	51093	622	53	26105	6280	55001	451
3,71		465	7	51061	610	59	25817	6333	55010	464
4,19		459	5	51076	617	56	26059	6348	54955	463
4,47		446	7	51108	519	63	25800	6340	55037	454
5,05		434	7	51125	586	57	25762	6398	55089	435
6,05		421	8	51127	566	44	25713	6450	55002	446
6,69		415	13	51137	571	49	25797	6574	55031	445

7,33		414	16	51167	573	47	25945	6611	55111	442
7,94		408	16	51162	574	48	25904	6673	55143	425
8,57		407	20	51190	569	44	25865	6669	55174	434
9,18		399	27	51189	561	43	25863	6739	55204	428
9,82		400	33	51202	569	44	25608	6737	55286	427
11,09		402	53	51211	564	44	25458	6763	55346	432
12,37		417	93	51245	559	50	25085	6691	55385	411
13,64		415	137	51231	563	43	24677	6726	55408	405
14,88		415	198	51239	567	47	24153	6799	55481	398
16,12		422	276	51220	559	45	23365	6762	55428	377
18,03		428	416	51138	558	34	21935	6765	55494	332
19,28		432	525	51061	565	37	20975	6734	55424	326

Table B.2: Raw data from gas chromatograph for parallel 2, NCF31-N

time on stream [h]	A He [uV*s]	A H2 [uV*s]	A O2 [uV*s]	A N2 [uV*s]	A ? [uV*s]	A CO [uV*s]	A CO2 [uV*s]	A ? [uV*s]	A C3H8 [uV*s]	A C3H6 [uV*s]
0,00			2561	51032					56299	
0,01	29	108	19	71038	750		1936	2737	247	
0,08	34	156	18	67995	733	57	8151	6041	6739	155
0,15	25	129	11	58520	613	147	16467	6608	33383	785
0,22	16	120	11	53501	578	184	20516	6803	47325	1085
0,29	14	119	12	51843	556	192	22012	6871	51949	1158
0,36	12	121	12	51393	558	193	22441	6868	53175	1160
0,43	8	128	7	51233	550	193	22533	6848	53686	1142
0,58		145	13	51102	556	181	23099	6952	53974	1118
0,02		150	8	51107	552	170	23548	7009	54035	1099
0,86		141	12	51065	542	170	23998	6983	54125	1089
1,01		151	8	51041	546	163	24426	6941	54098	1073
1,15		152	11	51023	550	161	24782	6987	54083	1066
1,29		149	8	51011	552	158	24843	6938	54090	1065
1,43		149	7	51001	556	158	24845	6946	54104	1051
1,65		142	6	50976	546	158	24956	6995	54115	1046
1,86		134	7	50990	556	158	25028	6977	54103	1033
2,07		137	4	51020	551	150	24929	6896	54219	1038
2,29		133	7	51026	549	153	24813	6892	54182	1025
2,50		133	7	51017	549	152	24898	6919	54204	1024
2,72		125	4	51015	534	143	24652	6918	54205	1021
2,93		129	7	51039	555	152	24827	6907	54226	1014
3,14		138	7	51036	556	143	24777	6886	54202	1006
3,35		131	6	51046	544	140	24754	6856	54238	999
3,57		129	7	51038	552	143	24800	6915	54269	1004
3,78		130	12	51055	559	141	24882	6955	54185	998
3,99		122	11	51030	550	136	24761	6872	54277	991
4,06		127	7	51050	550	137	24801	6897	54240	995
4,76		137	19	51039	529	124	24727	6949	54270	969
5,40		133	36	51040	540	136	24719	6974	54245	946
6,03		146	70	51049	552	118	24390	6933	54212	921

6,65		153	123	51009	536	124	23938	6952	54284	892
7,93		177	387	50913	493	60	22080	7085	54631	788
9,20		183	985	50676	489	22	16905	6913	54875	573
10,48		187	1783	50493	475	8	10093	6907	55384	259
11,71		188	2006	50509	462	12	7969	6940	55532	142
12,95		193	2036	50539	476	11	7681	6921	55605	152
14,21		192	2059	50562	459	10	7428	6797	55591	135
15,47		187	2072	50566	466	10	7390	6842	55699	134
16,73		192	2080	50557	450	7	7280	6805	55891	135
18,00		197	2103	50596	457	10	7122	6662	55715	147
19,28		195	2105	50566	463	6	7065	6520	55821	126
20,95		199	2130	50951	473	6	6953	2764	56121	140
21,02		200	2136	50988	469		6967	2493	56231	135
21,20		199	2137	51033	469		6931	2009	56220	129

Table B.3: Raw data from gas chromatograph for parallel 3, NCF31-N-900

time on stream [h]	A He [uV*s]	A H2 [uV*s]	A O2 [uV*s]	A N2 [uV*s]	A ? [uV*s]	A CO [uV*s]	A CO2 [uV*s]	A ? [uV*s]	A C3H8 [uV*s]	A C3H6 [uV*s]
0,00			2860	52174		2860	0		55349	0
0,01		137	28	72088	685				321	
0,08		124	24	69605	649		9211	243	6218	125
0,15		145	17	59724	573	112	17899	1791	33423	678
0,22		157	17	54368	509	138	22175	3379	47671	966
0,29		175	16	52462	497	148	23889	4350	52610	1063
0,37		189	13	51954	498	148	24275	4908	53822	1077
0,44		203	14	51774	500	140	24316	5280	54175	1077
0,51		205	15	51690	496	140	24547	5557	54301	1065
0,65		205	16	51608	492	131	24888	5927	54498	1048
0,80		202	13	51570	496	134	25282	6197	54586	1043
0,94		200	13	51521	471	128	1	6278	1	0
1,08		197	10	51518	497	132	25653	6376	54584	1031
1,22		200	16	51485	479	130	25771	6460	54648	1040
1,37		192	12	51477	498	127	25856	6525	54567	1022
1,51		191	14	51473	488	126	25944	6610	54578	1022
1,65		182	16	51481	480	128	26004	6685	54579	1021
1,86		185	9	51466	476	133	25923	6873	54684	1018
2,08		178	14	51476	494	117	25803	6874	54672	1012
2,29		186	12	51481	487	122	25963	6953	54750	1014
2,50		184	15	51489	484	120	25915	6999	54719	1012
2,71		178	11	51466	476	128	25897	7069	54637	1006
2,93		181	14	51478	484	123	25795	7072	54647	1008
3,07		179	13	51478	483	121	25905	7130	54750	1008
3,14		180	15	51484	482	125	25877	7108	54717	1008
3,78		186	30	51474	491	122	25884	7217	54707	992
4,42		195	89	51473	483	116	25182	7249	54761	969
5,04		206	260	51443	472	105	23922	7372	54981	922
5,67		220	663	51307	477	89	20495	7356	55166	801
6,31		226	1291	51105	467	60	14786	7374	55442	575
6,95		230	1846	50933	449	25	9702	7271	55704	358
7,59		247	2131	50864	463	14	6919	7354	55798	187
8,22		257	2215	50850	454	2	5983	7295	55895	165

8,84		256	2233	50818	453	5	5805	7463	55913	160
9,48		254	2252	50813	445	12	5660	7460	55903	135
10,12		256	2264	51033	459	7	5651	5236	56140	149
11,07		261	2285	51444	446	0	5644	1198	56640	144
12,03		259	2292	51478	457	0	5558	1149	56573	144
12,96		260	2298	51484	461		5509	1142	56664	129
13,92		264	2291	51483	471		5511	1100	56668	133
14,86		260	2314	51452	457		5472	1087	56606	130
15,80		263	2316	51435	469		5438	1068	56619	136
16,73		260	2300	51408	455		5426	1041	56569	130
17,69		258	2313	51419	462		5404	1061	56528	135
17,76		265	2320	51434			5403	1062	56631	137

Table B.4: Raw data from gas chromatograph for parallel 4, NCF29

t on stream [h]	A He [uV*s]	A H2 [uV*s]	A O2 [uV*s]	A N2 [uV*s]	A ? [uV*s]	A CO [uV*s]	A CO2 [uV*s]	A ? [uV*s]	A C3H8 [uV*s]	A C3H6 [uV*s]
0,00			2695	51112			0		55869	0
0,03		158	41	71596	670			160	265	
0,10		215	358	68852	661		4559	866	7659	20
0,17		142	1190	58922	552		6248	1469	34997	160
0,24		99	1647	53744	499		7290	1876	48827	285
0,31		77	1830	51915	487		7679	2172	53329	402
0,38		63	1861	51426	492	42	8129	2419	54457	427
0,46		52	1851	51272	481	43	8446	2654	54720	473
0,53		54	1831	51168	473	48	8815	3038	54869	502
0,60		52	1791	51126	467	48	9146	3378	54818	521
0,74		48	1731	51087	481	48	9718	3693	54913	574
0,88		49	1666	51085	477	49	10341	3930	54746	606
1,02		50	1599	51085	479	51	10933	4161	54833	636
1,17		45	1532	51113	478	43	11461	4378	54751	661
1,31		42	1478	51114	475	47	12031	4516	54784	694
1,45		53	1432	51098	472	45	12653	4729	54742	712
1,62		49	1370	51115	474	47	13059	4878	54750	737
1,77		47	1327	51134	467	46	13580	5097	54760	750
1,91		49	1276	51134	468	50	13984	5241	54739	769
2,05		46	1244	51147	469	49	14413	5325	54709	778
2,19		49	1210	51141	459	47	14725	5576	54730	798
2,34		52	1179	51143	466	43	15026	5799	54724	806
2,55		52	1143	51133	467	46	15496	5826	54796	817
2,89		53	1113	51128	455	46	15824	5952	54655	842
3,17		50	1091	51163	460	47	15963	6059	54725	856
3,25		55	1085	51184	472	49	16067	6213	54790	872
3,88		57	1067	51122	471	45	15810	6196	54682	894
4,52		54	1101	51022	473	59	15588	6173	54666	914
5,15		55	1137	50958	474	56	15297	6183	54665	942
5,78		51	1168	50944	467	54	14907	6194	54598	954
6,41		54	1209	50943	465	61	14537	6096	54650	965
7,37		54	1254	50949	463	57	14039	5934	54729	985
8,31		66	1304	50974	456	62	13639	5683	54750	988

9,26		59	1349	50998	461	58	13213	5537	54973	997
10,20		61	1394	51053	461	59	12642	5370	54921	986
11,16		69	1433	51083	454	58	12333	5215	55127	979
12,11		70	1476	51110	450	59	11960	5059	55192	991
13,03		72	1503	51126	461	56	11667	4938	55224	974
13,99		75	1533	51128	465	57	11313	4831	55217	962
14,95		78	1568	51106	445	57	10998	4711	55147	959
15,90		79	1593	51058	459	53	10712	4715	55039	951
16,86		75	1620	51043	458	55	10482	4577	55127	943
17,53		82	1641	51030	462	58	10349	4579	55074	932
17,67		86	1638	51030	469	58	10205		54939	931
18,29			1661	51185	444	52	10203		55025	908

Table B.5: Raw data from gas chromatograph for the blank test

t on stream [h]	A He [uV*s]	A H2 [uV*s]	A O2 [uV*s]	A N2 [uV*s]	A ? [uV*s]	A CO [uV*s]	A CO2 [uV*s]			A C3H8 [uV*s]	A C3H6 [uV*s]
0,00		0		240		0	0		?	0	0
0,01		209	33	71908	653			157	317	262	
0,08		311	459	69647	639			149	260	6089	
0,15		273	1632	59486	530			160	279	34054	
0,22		258	2258	53956	479			145	255	49213	
0,36		243	2627	51481	453			147	266	55840	
0,50		230	2675	51262	462			143	278	56291	
0,64		235	2680	51193	457			131	270	56426	
0,79		235	2660	51222	454			134	266	56424	
0,93		235	2650	51226	457			156	289	56582	
1,22		235	2645	51239	456			135	287	56613	
1,57		236	2649	51258	447			142	301	56239	
1,93		228	2651	51262	466			142	291	56563	
2,29		233	2644	51228	469			137	277	56444	
2,64		231	2649	51234	450			144	299	56578	
3,00		234	2638	51244	461			145	290	56390	
3,36		230	2637	51247	463			146	273	56454	
3,71		234	2645	51247	454			136	283	56361	
4,17		233	2643	51252	466			143	272	56385	
5,13		230	2645	51270	463			141	292	56451	
6,08		228	2653	51284	452			142	290	56406	
7,04		237	2643	51293	453			138	295	56482	
8,00		237	2652	51317	451			136	279	56539	
9,57		232	2653	51331	442			123	260	56544	
11,17		234	2647	51383	452			122	272	56817	
12,74		234	2652	51442	438			110	245	56795	
14,33		240	2652	51468	440			109	241	56922	
15,90		232	2638	51500	436			103	238	57002	
17,44		239	2654	51522	446			88	201	57004	
19,04		236	2654	51513	430			91	201	57006	
21,91		228	2654	51561	432			93	233	56959	

Table B.6: Raw data from gas chromatograph for Vulcan carbon

time on stream [h]	A He [uV*s]	A H2 [uV*s]	A O2 [uV*s]	A N2 [uV*s]	A ? [uV*s]	A CO [uV*s]	A CO2 [uV*s]	?	A C3H8 [uV*s]	A C3H6 [uV*s]	t on stream [h]
7,72				251		0	0		0	0	7,72
7,72	370			70931	183		781		228		7,72
7,72	433	61	385	68560			876		6352		7,72
7,72	260	94	1394	58656	136		266		33945	24	7,72
7,72	145	130	2173	51324	111	14	854		54155	40	7,72
7,72	57	155	2294	50508	92	9	1177		55970	34	7,72
7,72	23	133	2298	50559	100	11	1081		56158	37	7,72
7,72	18	139	2283	50493	108	13	972		56115	48	7,72
7,72		157	2391	50552	104	10	4155		56362	130	7,72
7,72	5	159	2403	50614	157	15	987		56325	134	7,72
7,72	17	210	2408	51117	531	11	4011	260	56363	142	7,72
7,72	13	213	2428	51106	547	18	4001	257	56350	135	7,72
7,72	8	205	2458	51082	542	15	3971	252	56418	138	7,72
7,72	10	218	2466	51092	547	15	3852	242	56401	167	7,72
7,72		226	2469	51086	547	14	3854	230	56421	167	7,72
7,72		229	2470	51070	547	16	3870	238	56476	158	7,72
7,72		226	2481	51086	551	18	3812	231	56301	176	7,72
7,72		228	2474	51064	547	14	3823	228	56413	174	7,72
7,72		230	2468	51080	542	16	3815	240	56411	169	7,72
7,72		232	2477	51069	518	19	3772	250	56427	171	7,72
7,72		228	2474	51042	518	17	3759	246	56448	175	7,72
7,72		233	2487	51087	510	16	3704	254	56379	221	7,72
7,72		234	2485	51083	506	18	3772	253	56595	200	7,72
7,72		240	2478	51078	515	22	3690	249	56526	197	7,72
7,72		244	2485	51104	516	20	3651	246	56503	201	7,72
7,72		250	2485	51108	512	16	3651	246	56503	204	7,72
7,72		251	2487	51090	520	17	3664	260	56530	225	7,72
7,72		254	2491	51106	504	15	3683	255	56584	236	7,72
7,72		261	2485	51099	505	16	3709	268	56610	240	7,72
7,72		263	2480	51113	515	16	3706	274	56591	223	7,72
7,72		262	2488	51094	508	15	3684	262	56629	251	7,72
7,72		257	2482	51091	501	18	3607	265	56567	240	7,72
7,72		268	2485	51095	502	16	3634	264	56541	233	7,72

7,72		259	2488	51101	515	18	3621	281	56470	263	7,72
7,72		262	2485	51096	515	14	3664	264	56549	256	7,72
7,72		268	2489	51073	517	15	3619	268	56558	262	7,72
7,72		265	2484	51074	528	17	3658	278	56595	263	7,72

Appendix C – ODH results

The conversion and selectivity for Vulcan Carbon are given in figure B.1.. Two plots are included in each figure, and the blue diamonds represent the full scale plot, whilst the red squares represent the scaled version of the same plot.

The selectivity for CO, CO₂ and H₂O was too low to calculate.

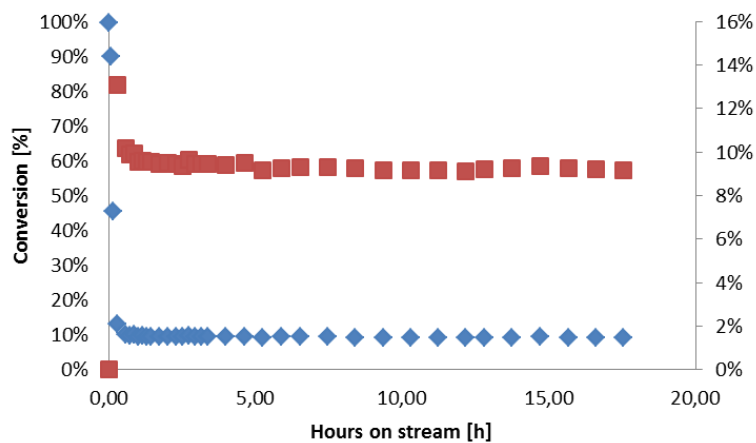


Figure C.1: Conversion of propane for Vulcan Carbon. The blue diamonds represent the full scale plot, and the red squares shows a scaled version of the same plot.

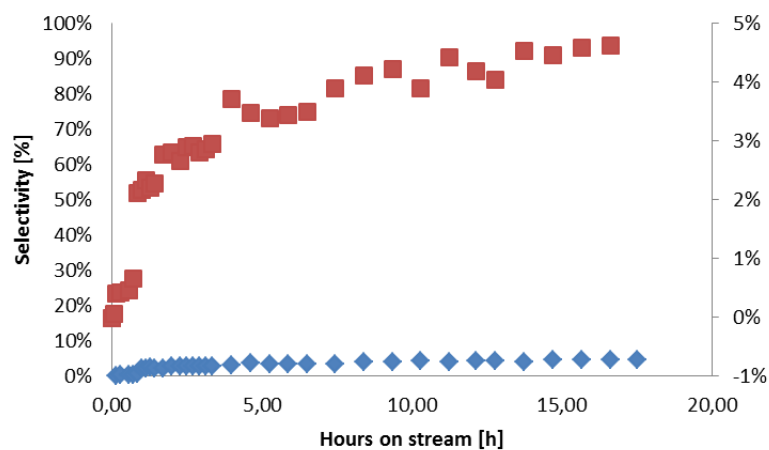
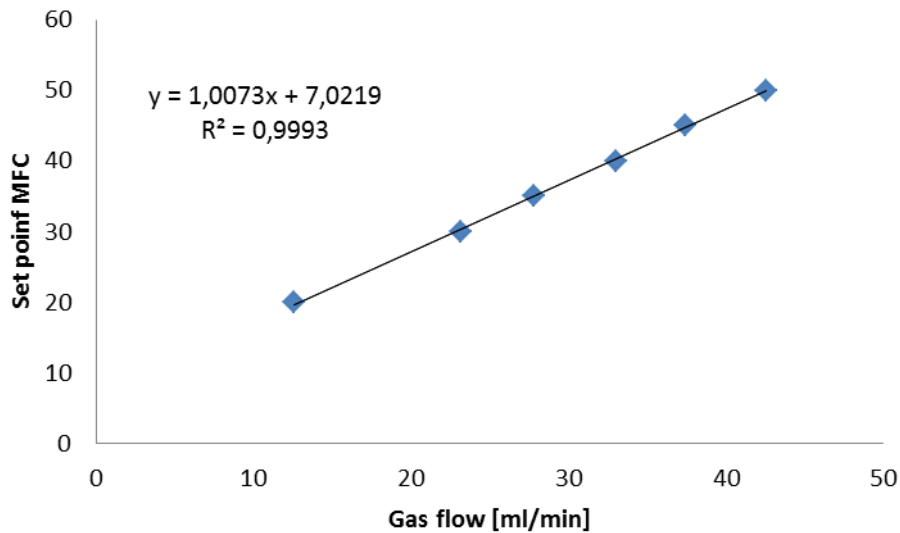


Figure C.2: Selectivity for propane for Vulcan Carbon. The blue diamonds represent the full scale plot, and the red squares shows a scaled version of the same plot.

Appendix D - Mass flow controller calibrations

The mass flow controllers were calibrated by using a soap bubble flow meter. The resulting graphs for propane, air, argon and nitrogen are shown in figure D1 to D4 respectively. The equations and R-values for the trend lines are also given in the figures.



Figur D.1: MFC calibration, propane

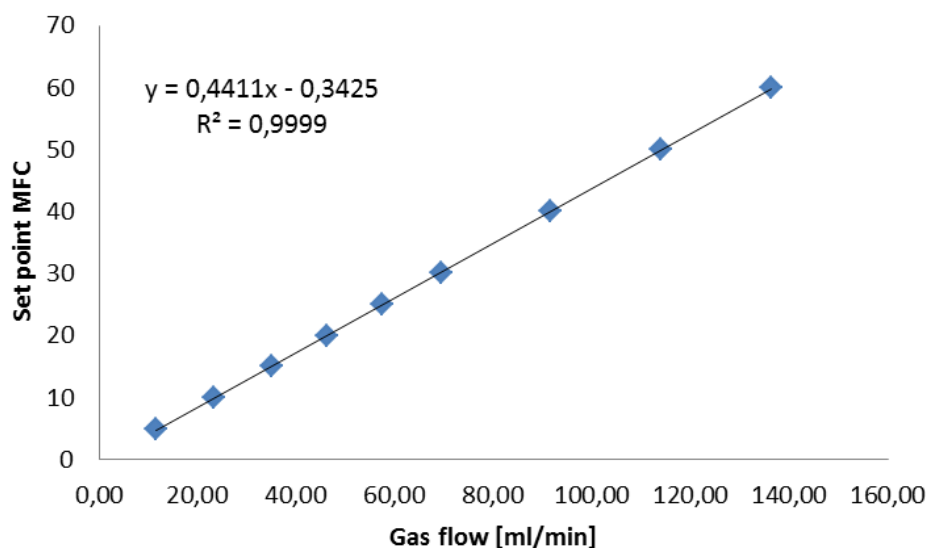


Figure D.2: MFC calibration, Synthetic Air

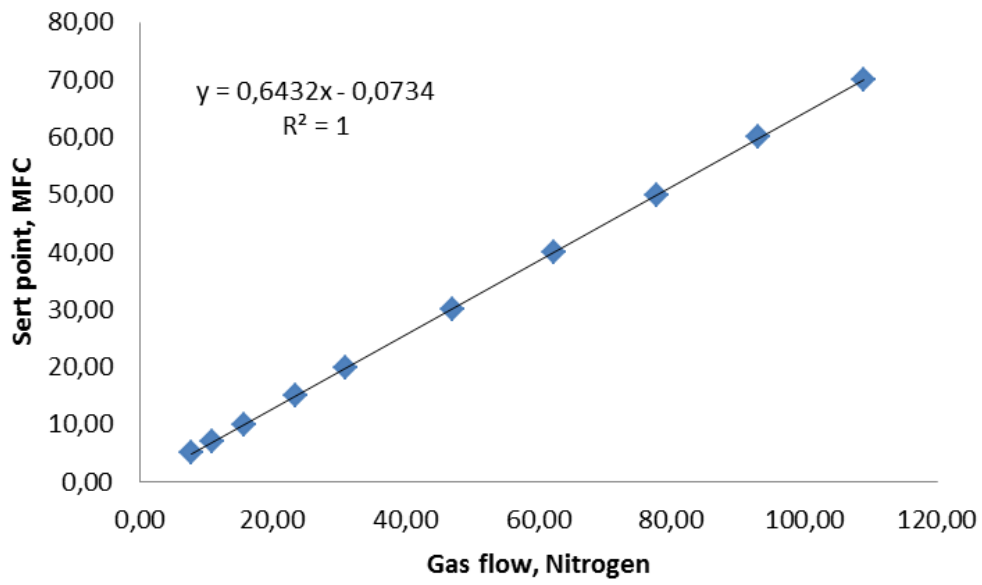


Figure D.3: MFC calibration, Nitrogen, upper MFC

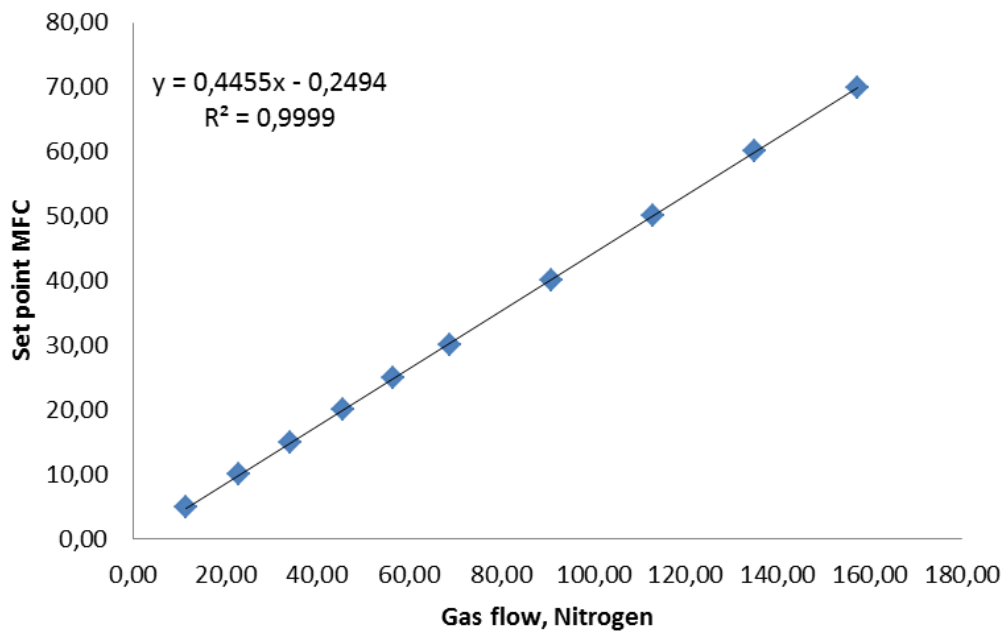


Figure D.4: MFC calibration, Nitrogen, lower MFC

Appendix E - Calibration curves and response factors

The volume percentages and the corresponding areas from the GC for nitrogen are shown in Table E1.

Table E.1: Volume percentages and corresponding areas from the GC for nitrogen
Nitrogen

Vol %	Area
57	40978,64
69,8	50188,81
86	61396,15
89,4	64322,99
2,94	2054,116

Volume percentage and GC area for nitrogen are plotted against each other in Figure E.1.

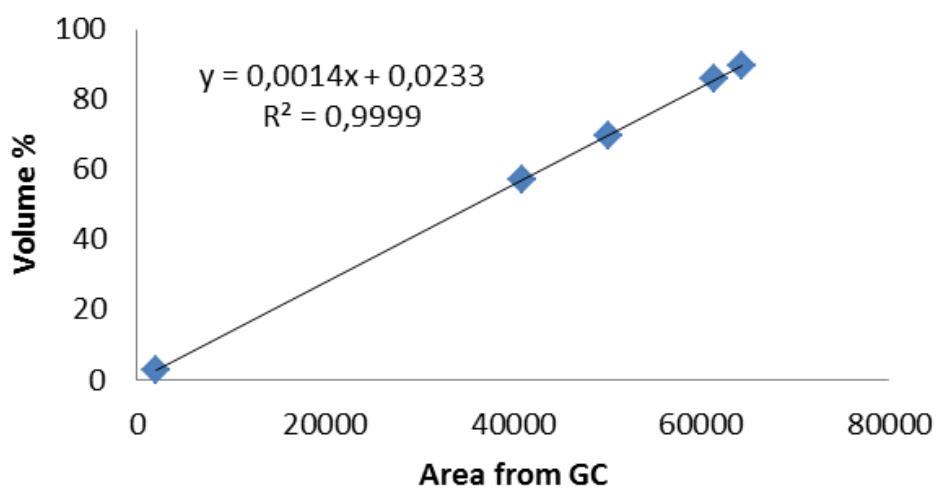


Figure E.1: Calibration curve for nitrogen

The volume percentages and the corresponding areas from the GC for propane are shown in Table E.2.

Table E.2: Volume percentages and corresponding areas from the GC for propane

Propane		Nitrogen	
Vol %	Area	Vol %	Area
0,2	404,53599	69,8	50188,81
10	21864,48779	89,4	64322,99
0,1035	217,89283	2,94	2054,116

Volume percentage and GC area for nitrogen are plotted against each other in figure E.2.

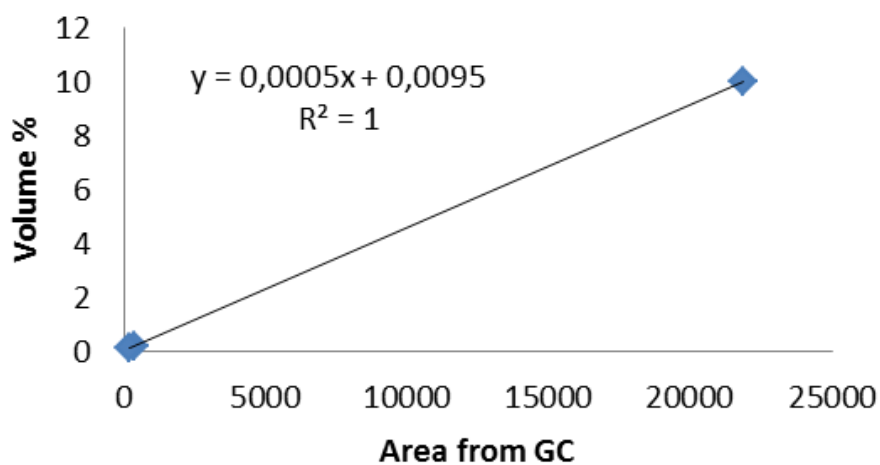


Figure E.2: Calibration curve for propane

The volume percentages and the corresponding areas from the GC for propene are shown in Table E.3.

Table E.3: Volume percentages and corresponding areas from the GC for propene

Propene		Nitrogen	
Vol %	Area	Vol %	Area
10	21097,63	69,8	50188,81
0,2	445,3634	89,4	64322,99
0,1029	211,9831	2,94	2054,116

Volume percentage and GC area for propene are plotted against each other in figure E.3.

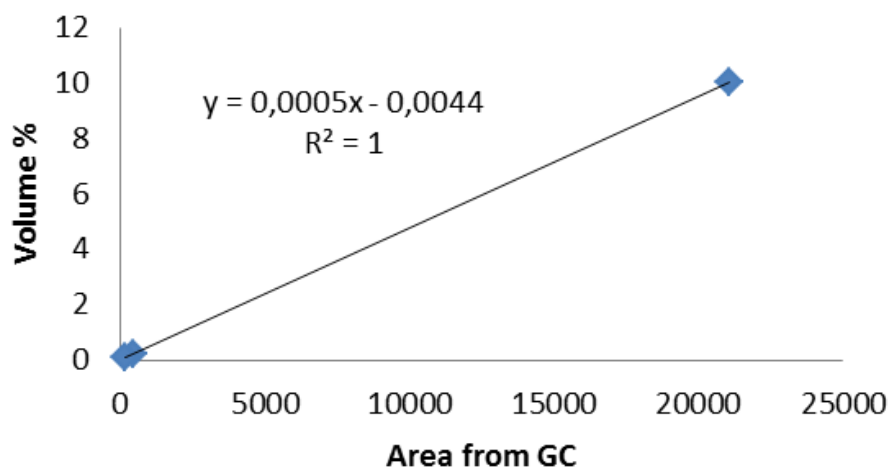


Figure E.3: Calibration curve for propene

The volume percentages and the corresponding areas from the GC for CO are shown in Table E.4.

Table E.4: Volume percentages and corresponding areas from the GC for CO

CO		Nitrogen	
Vol %	Area	Vol %	Area
3	1995,183	69,8	50188,81
1	791,7039	89,4	64322,99
30,8	20684,49	2,94	2054,116

Volume percentage and GC area for CO are plotted against each other in figure E. 4.

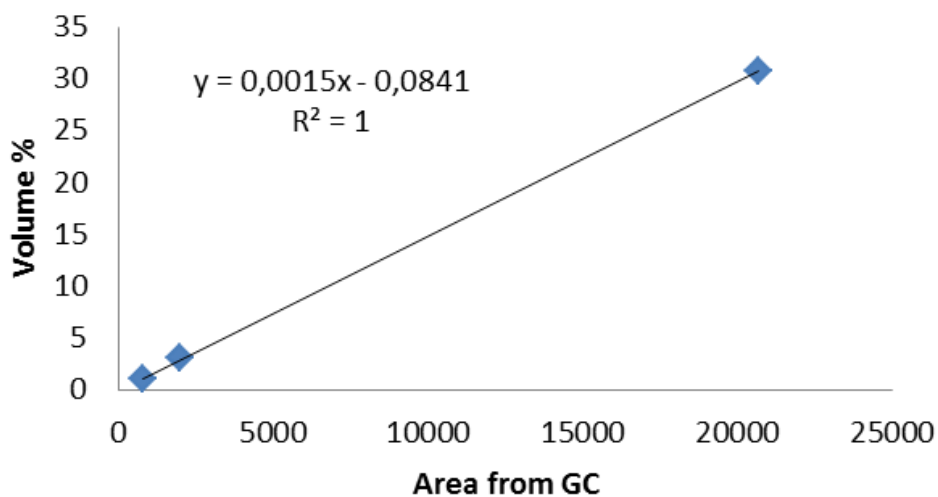


Figure E.4: Calibration curve for CO

The volume percentages and the corresponding areas from the GC for CO₂ are shown in Table E.5.

Table E.5: Volume percentages and corresponding areas from the GC for CO₂

CO ₂		Nitrogen	
Vol %	Area	Vol %	Area
5	57993,48	69,8	50188,81
1	14315,43	89,4	64322,99
0,495	6395,187	2,94	2054,116

Volume percentage and GC area for CO₂ are plotted against each other in figure E.5.

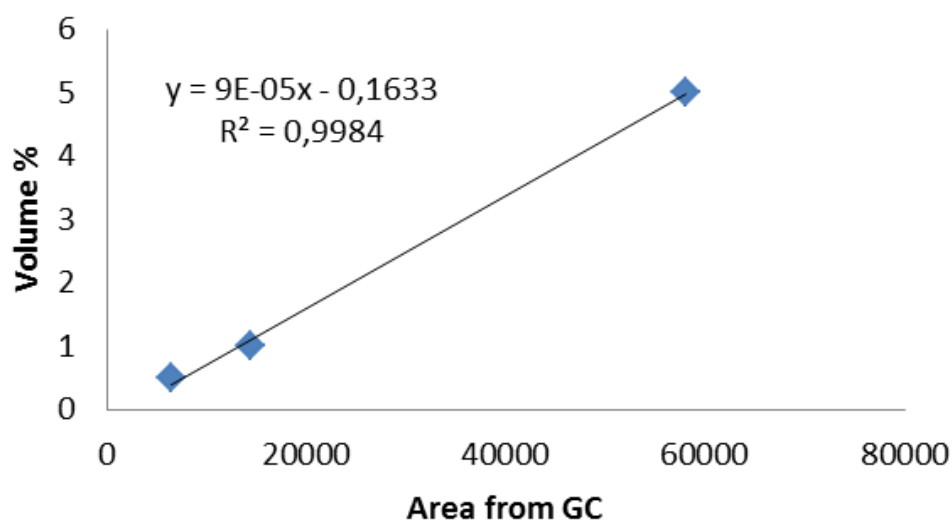


Figure E5: Calibration curve for CO₂

The volume percentages and the corresponding areas from the GC for CO₂ are shown in Table E.6.

Table E.6: Volume percentages and corresponding areas from the GC for Synthetic Air

Synthetic Air		Nitrogen	
Vol %	Area	Vol %	Area
20,8	16929,12	69,8	50188,81
0	0	89,4	64322,99

Volume percentage and GC area for synthetic air are plotted against each other in figure E.6.

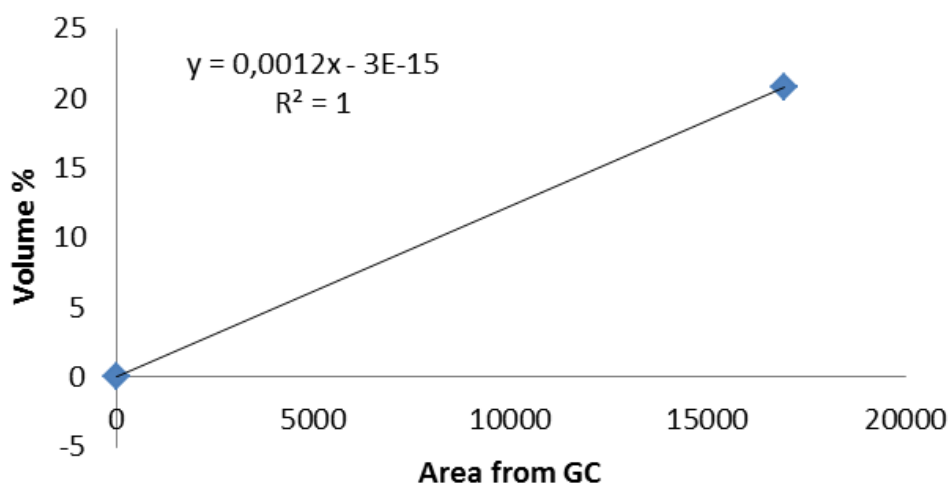


Figure E.6: Calibration curve for propene

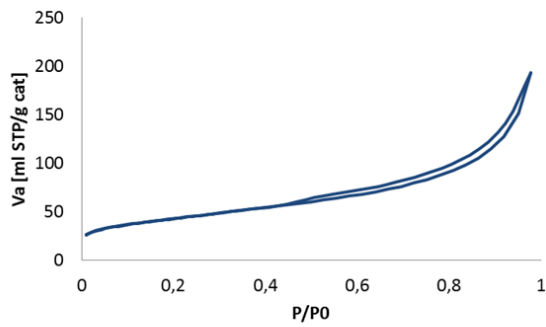
The response factors for the different gases are given in table E.7.

Table E.7: Response Factors for the different gases

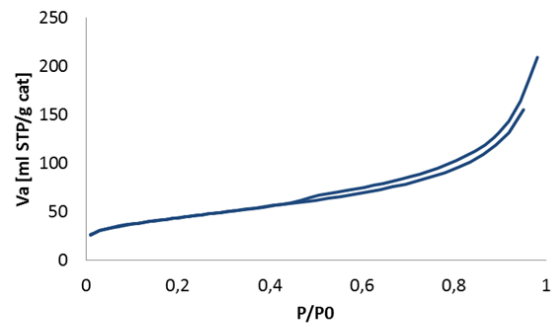
Response factors	
Propane	2,955025585
Propene	2,992554092
CO	0,995498777
CO ₂	18,17291289
Synthetic air	1,131929905

Appendix F – BET-Isotherms

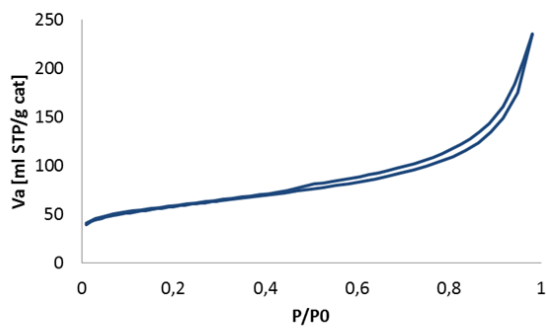
The isotherms for two parallels of BET measurements NCF31, NCF31-N and NCF31-N-900 are given in Figure F.1.



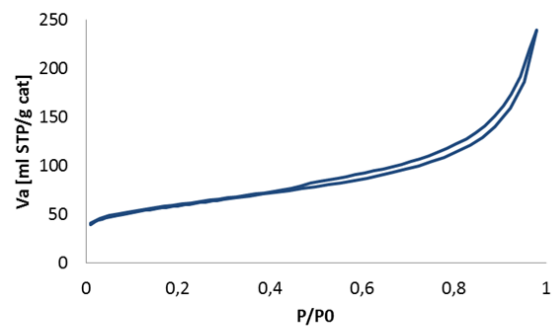
a) NCF31, Parallel 1



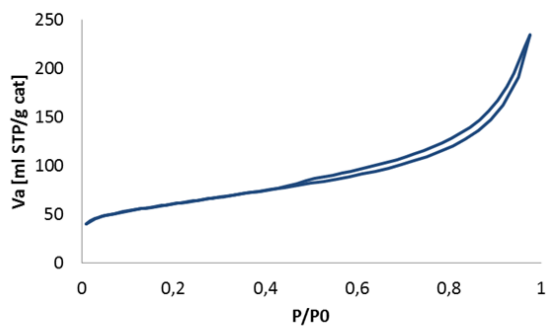
b) NCF31, Parallel 2



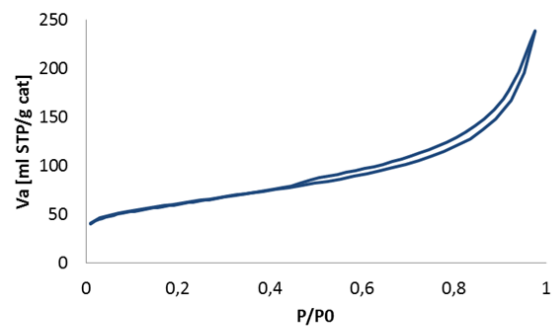
c) NCF31-N, Parallel 1



d) NCF31-N, Parallel 2



e) NCF31-N-900, Parallel 1



f) NCF31-N-900, Parallel 2

Figure E.1: BET isotherms for 2 parallels of BET scans for NCF31 (a, b), NCF31-N (c, d) and NCF31-N-900 (e, f).